POLITECNICO DI MILANO

Facoltà di Ingegneria Industriale e dell'Informazione

Corso di Laurea Magistrale in Ingegneria Elettronica

PARTICULATE MATTER DETECTOR BASED ON IMPEDANCE SENSING

Relatore: Prof. Marco SAMPIETRO
Correlatore: Ing. Marco CARMINATI

Tesi di Laurea Magistrale di:
Lorenzo PEDALA'
Matricola: 769858

Anno Accademico 2012-2013

Contents

List of Figures

List of Tables

Abstract

Impedance measurement is successfully employed in various fields to sense single particle events, e.g. for cells counting. This kind of detection works together with a fluidodynamic system, which properly drives the particles to be sensed. Airborne Particulate Matter, which is the collection of micro and nano particles suspended in the outside air, has been related to several human diseases (cardiovascular diseases, lungs cancer) ; its concentration must be constantly monitored, to effectively implement pollution contrasting policies.

A novel PM detector, based on impedance measurement, is proposed in this thesis work. The project conjugates the design of an electronic impedance detection system, which was carried out in the electronics laboratory led by Prof. Marco Sampietro at DEIB, Politecnico di Milano, and the design of a microfluidodynamic system, which was carried out by the colleagues of LaBS, Politecnico di Milano; they also managed the electrodes manufacturing process, which took place at the École Polytechnique Fédérale de Lausanne. My tasks were the design of a proper sensor and of the analog front-end; their electronic characterization; their use along with a commercial lock-in instrument to actually perform PM detection.

After an introduction on particulate matter, its consequences on health, and the standard measurements techniques, the system architecture is outlined in Chapter 1. Chapter 2 deals with the sensor design stages, from Finite Elements simulations, during which different geometries were studied, to the final wafer layout. Chapter 3 describes the design a low-noise front-end stage, with two possible improved variants. Chapter 4 faces the characterization of the capacitive sensors and of the front-end circuit, particularly for the noise performances. They were finally tested along with the external lock-in. For the first time the detection of PM10 by impedance sensing was demonstrated (in static and dynamic conditions), as shown in Chapter 5.

Sommario

Le misure di impedenza vengono impiegate con successo in vari ambiti per rilevare eventi associati a singole particelle, ad esempio per il conteggio di cellule. Questo tipo di misura viene realizzato assieme a un sistema fluidodinamico, il quale veicola opportunamente le particelle in questione. Il particolato atmosferico, ovvero l'insieme delle micro e nano particelle sospese nell'atmosfera, è stato posto in relazione a numerose patologie (malattie cardiovascolari, tumore polmonare); la concentrazione di particolato deve essere costantemente monitorata, per attuare efficacemente politiche di contrasto dell'inquinamento.

Un nuovo tipo di rilevatore di particolato, basato su misure di impedenza, viene presentato in questa attività di tesi. Il presente lavoro coniuga il progetto di un sistema elettronico di rilevamento, realizzato all'interno del laboratorio di elettronica diretto dal Prof. Marco Sampietro presso il DEIB del Politecnico di Milano, e il progetto di un sistema micro-fluidodinamico, realizzato dalle colleghe e dai colleghi del LaBS del Politecnico di Milano, che hanno curato anche il processo produttivo degli elettrodi, effettuato presso la École Polytechnique Fédérale de Lausanne. Mi sono occupato del progetto di un sensore adatto allo scopo, e del front-end analogico; della loro caratterizzazione elettronica; di effettuare realmente misure di particolato affiancando un demodulatore lock-in commerciale.

Nel Capitolo 1, dopo un'introduzione sul particolato atmosferico, sulle sue conseguenze sulla salute umana, e sulle attuali tecniche standard di rilevamento, viene delineata un'architettura generale per il sistema. Il Capitolo 2 riguarda le fasi di progetto del sensore, dalle simulazioni a elementi finiti, durante le quali sono state considerate diverse geometrie, al layout finale del wafer. Il sensore capacitivo è stato realizzato tramite accoppiamento di elettrodi metallici coplanari, in modo tale da massimizzare il campo elettrico nel volume sensibile, e quindi la corrente di segnale al passaggio del particolato. Altre geometrie sono state considerate, ad esempio elettrodi a facce piane parallele; tuttavia, a causa di limiti tecnologici e di semplicità nel progetto fluidodinamico, la configurazione planare è stata preferita. Sono state studiate approfonditamente le dipendenze del segnale capacitivo dai parametri geometrici degli elettrodi, tramite simulazioni a elementi finiti. Il layout definitivo viene quindi descritto dettagliatamente, motivando le scelte dei parametri.

Il Capitolo 3 descrive il progetto di un front-end a basso rumore, e di due possibili varianti a prestazioni più elevate. Il progetto più semplice consiste di un classico transimpedenza con capacità in retroazione. I fattori concorrenti nel determinare il rapporto segnale rumore vengono individuati, in modo tale da definire l'intervallo di frequenze per cui esso è massimo; esso risulterà limitato dal rumore serie dell'operazionale, che viene amplificato da tutte le capacità af-

ferenti al nodo invertente dell'operazionale; questo risultato sarà determinante nella scelta dell'operazionale. Possibili miglioramenti si raggiungono aggiungendo un induttore che risuoni con le capacità sopra citate, per abbassare il contributo del rumore serie. Infine, prendendo spunto dall'operazionale scelto per la realizzazione dell'integratore, si è studiato un front-end a due stadi, caratterizzato da un preamplificatore a JFET di elevate prestazioni.

Il Capitolo 4 affronta la caratterizzazione dei sensori capacitivi e del circuito di acquisizione, in particolare per quanto riguarda le prestazioni di rumore. Le misure riguardanti il front-end e i sensori progettati risultano conformi alle aspettative. Infine viene studiato il sistema complessivo, in cui la demodulazione lock-in è effettuata da uno strumento commerciale, che campiona l'uscita del transimpedenza, e la filtra con un riferimento generato internamente, che ovviamente è pure applicato al sensore. Il rumore dovuto al riferimento sinusoidale si rivela limitante, per cui si è optato per una configurazione di misura differenziale, già prevista nel progetto del front-end. Si ottiene una sensibilità minima di due atto Farad, nelle condizioni migliori di misura.

Per la prima volta si è dimostrato il rilevamento di PM10 tramite misure di impedenza (in condizioni statiche e dinamiche), come mostrato nel Capitolo 5. Per quanto riguarda le misure statiche, si è riusciti nell'intento di rilevare sfere di plastica delle dimensioni di 10 μm opportunamente posizionate. Successivamente, tramite una camera microfluidica applicata sui sensori, sono state rilevate le variazioni capacitive prodotte da una sospensione aerea ti talco industriale, di dimensioni medie pari a 8 μm. Gli esperimenti effettuati con il sistema realizzato sono descritti facendo riferimento a fotografie di immagini al microscopio, che concordano e giustificano le forme d'onda rilevate nel tempo.

Chapter 1

Particulate matter detection

1.1 Particulate matter

Dust, industrial soot, car exhaust, dead skin shreds, bacteria: these are all constituent of the so-called *particulate matter* (PM). Airborne particulate matter is a mixture of heterogeneous solid and liquid particles suspended in the air [1]. These particles originate from both natural sources and industrial processes, and even people generate them: a sitting human being releases about 100 000 skin particles per minute. Several health, environmental, and manufacturing issues are related to the PM distribution, therefore a continuous monitoring and characterization activity is carried out.

Some living beings emit inert organic particles (generally carbon-based), while others *are* viable organic particles, like bacteria and fungi; inert inorganic particles form the remaining part of PM. The chemical composition, which concurs in determining the way particulate matter affects the environment, evidently covers a very wide range. Experimental results [2] show that in the urban area of Milan, Italy, a large fraction of PM is composed by sulphates, and crustal and combustion elements (Si, Fe, Al, Ca, Pb, Zn, Cu, K, Ni, Cr,), the latter being in the form of oxides; another substantial portion of particulate matter includes carbon and nitrogen compounds.

As the particle composition displays a broad variability, so does the size distribution. Particulate matter classification defines two main classes, based on size: PM_{10}, i.e. particles having a maximum 10 µm size, and the analogue $PM_{2.5}$ and PM_1. Particles less than 100 nm are called *ultrafine*, while those greater than 10 µm form the *coarse* fraction. Even the notion of size yields to some ambiguity, because these bits, scraps, lumps, (microorganisms!) display the most random and irregular shapes. One could define size, e.g., as the maximum Feret's diameter, which is the distance between the two parallel lines that restrict the object's projection on a particular plane [3].

Generally, the *aerodynamic diameter* is referred to as the particle's size. It is defined as the diameter of a unitary density sphere, having the same terminal settling velocity as the original particle [4]. It proves useful for those particles larger than 0.5 µm, which experience a substantial inertia. The smaller ones, instead, remain suspended in the air in Brownian motion; their equivalent diameter is the *diffusive diameter*, that of a sphere having the same diffusion

coefficient.

The particles composition varies with size. Sulphates appear mainly in the $PM_{2.5}$, while crustal elements are more present in the interval between PM_{10} and $PM_{2.5}$, for example. Size also affects the PM concentration in the air. Airborne particles show a size distribution of (diameter)$^{-\alpha}$, where α is about 2, which is coherent with the fact that the smaller fraction remains suspended in Brownian motion.

1.2 PM issues

Pollutants produced by anthropogenic combustion processes constitute a significant fraction of particulate matter [5], especially of $PM_{2.5}$. Their primary role on early deaths due to poor air quality has been acknowledged by the U.S. Environmental Protection Agency: in 2010 there were 160 000 premature deaths in the U.S. due to $PM_{2.5}$ exposure. Electric power generation; industry; commercial and residential combustion; road, rail, and marine transportation; these have been identified as the main sources of polluting $PM_{2.5}$, which has been associated to premature deaths due to cardiovascular diseases and lung cancer.

Sulfates are among the pollutants deriving from coal power plants and from marine transportation, while road vehicles exhaust are responsible for nitrates emissions. Road transportation holds the largest share of the total premature deaths for $PM_{2.5}$, even exceeding the car accidents fatalities in 2005 (U.S.A.). U.S. and European studies showed an excess risk of 1% for cardiovascular diseases per $10\,\mu g/m^3$ PM_{10} increase [1]. Particulate matter has also been associated with asthma, bronchitis, and even a promotion of allergic sensitization, and exacerbation of allergic responses.

PM-related diseases depend on both size (smaller particles penetrate deeper into lungs, eventually passing through the circulatory system) and chemical composition (which affects the way PM vehiculates toxic molecules) [6]. Most of the studies on PM_{10} levels show higher levels than the air quality standards of U.S. and Europe [1], which have been fixed at $50\,\mu g/m^3$ and $150\,\mu g/m^3$, respectively.

Particulate matter also affects industrial processes performances that require high cleanliness, therefore a constant level monitoring is mandatory. Electronic IC manufacturing is a suited example: particles of the order of 10 nm must be filtered to avoid failures. PM is a concerning issue for pharmaceutical industries, too, which must ensure that parenteral drugs do not contain potentially infecting external bodies. They typically require process cleanliness levels of $0.5\,\mu m$.

1.3 Standard detection methods

The easiest way to measure PM levels is the *gravimetric* method. A polluted-air flux is forced onto a filter, which gathers all the PM particles which can get trapped. The total mass is weighted, and, being known the total pumped air volume, the average concentration can be calculated. Although being the only accepted technique for instruments certification, it is a very slow process, which provides information *a posteriori*. It cannot be employed to measure neither single particles size, nor chemical composition, which are the interesting features

from a toxicological point of view.

The particles accumulated on a filter can also be analyzed through *Ion Beam Analysis* (IBA) [7]. A beam of accelerated ions is focused on the filter, thus producing a certain kind of particles to be analyzed. Although single particles discrimination cannot be performed, this method allows to identify the chemical composition of the sample, and to evaluate their concentration into the overall mass. *Particle Induced X-ray Emission* (PIXE) measures the X-rays emitted after ion collision, and it can detect those elements with Z greater than 10. *Particle Induced γ-ray Emission* (PIGE) and *Particle Elastic Scattering Emission* are employed to measure lower-atomic-number particles; the former detects the emitted γ-rays, the latter relies on the collision between the incident ions and the sample's nuclei [7]. These methods are generally complemented by an impactor, which sorts the particles in size classes, so that information on both size and composition is available.

The only commercial technique able to sense single particles is *Laser Scattering*. A laser beam interacts with the PM-polluted air to be analyzed, which is properly focused as a narrow stream. When a single particle crosses the laser beam, a certain amount of light (which, under certain hypothesis, depends on the sixth root of the particle's diameter) gets reflected. In this way, single particles transit events can be detected, and the particle's size can be estimated, for it determines the quantity of reflected power. Particles up to 300 nm can be sensed.

1.4 Impedance measurements

Impedance measurement is a very powerful instrument for single particle sensing. It is successfully employed to detect cell transit events, thus providing a non-invasive counting technique [8]. A capacitive or resistive (or both) sensor is stimulated by an electrical variable, for example voltage. The constitutive relation of the sensor determines the dual electrical variable (current in this case), which is constantly monitored. As the external particle flows near the sensor, it perturbs the sensor's impedance, thus changing the sensor's current during its transit. The impedance variation, whose amplitude and phase depend on the particle's electrical properties, can be detected, according to the reading circuit's sensitivity. A binary piece of information is obtained, dealing with the particle's presence or absence; some peculiar properties of the particle can be also observed, by measuring the amount of amplitude and phase variations.

Impedance measurements are commonly performed by lock-in demodulation. It is a synchronous filtering [9]: when a sinusoid is multiplied by an another one, having the same frequency, a DC component, along with the second harmonic arise:[1]

$$A\cos(\omega_0 t + \phi_0)B\cos(\omega_0 t) = \frac{AB}{2}\cos(\phi_0) + \frac{AB}{2}\cos(2\omega_0 t + \phi_0)$$

The second harmonic is low pass filtered; the low frequency value is maximum when the two sinusoids have no phase difference; viceversa, it is null when

[1] If the current signal is amplitude modulated, its envelope gets translated at DC, thus occupying a finite low-pass bandwidth.

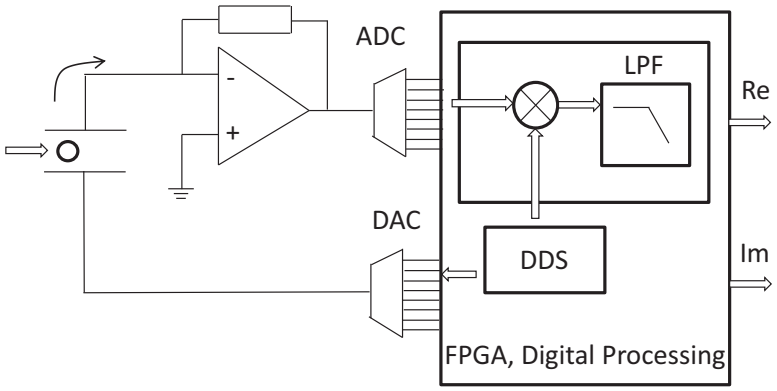

Figure 1.1: Acquisition and lock-in processing circuit for PM impedance sensing.

they're in quadrature. The sensor's impedance may introduce a phase shift, thus producing a current with real and imaginary part. By performing two simultaneous demodulations with two orthogonal references, both real and imaginary part can be measured, so the phase shift and the amplitude of the sensor impedance (or of its variations) can be evaluated.

Some important benefits derive from the fact that the current signal is sinusoidal, so its frequency can be chosen beyond the $1/f$ noise corner frequency of the reading circuit; furthermore, the low pass filter bandwidth can be chosen independently from the reference frequency, which is a great advantage with respect to resonant band-pass filters.

Perhaps, impedance sensing may be used for PM detection, too.

1.5 An alternative PM detection system

A complete PM detector based on impedance sensing is shown on figure 1.1. The particle flowing near the sensor, thanks to a *micro-fluidodynamic* system, induces a current signal, which is read by an analog front-end. The analog signal is then converted into digital form; a digital system relying on a *Field Programmable Gate Array* FPGA unit performs the digital lock-in, and provides the sinusoidal reference by means of a *Direct Digital Synthesizer* (DDS) [10]. A capacitive-like impedance measurement would be suited for air measurement.

This instrument is expected to be able to compete with the standard PM detectors, in terms of single particles sensitivity; the ultimate goal would be to both perform particles counting, and size sorting, which proves critical for human health issues. The compactness and low cost of impedance detectors would make this instrument rather attractive, even though its sensitivity did not reach the level of standard PM counters. A PM detection global network may be realized, with several fixed stations located in urban areas, sharing information through wireless transceivers. The easy size reduction provided by integrated circuits, along with MEMS technologies, might produce a complete system-on-chip where both electronics and microfluidics would coexist on the same IC, which could be included in today's smartphones as a portable PM detector.

Chapter 2

Sensor design

2.1 General considerations

The way particulate matter interacts with the sensor is expected to be strongly dependent on the geometry of both the PM particle and the sensing electrodes, beside their material. Two geometrical approaches can be followed: the particles might flow between the plates of a parallel-plate capacitor; the particles might flow, or might be deposited, above a coplanar electrodes pair, in contact to or very close to the sensor surface.

Another free parameter is the fluid that conveys the particles: PM could remain in the air, or it could be separated from it and added to a liquid medium. The former strategy would result in a more compact, practical, and easy-to-use device: a future development of a fully integrated microfluidic and electronic system, which could be one of the several applications of nowadays smartphones, would rather use this option, without any liquid and bulky pumping systems involved. On the other hand, the latter strategy would simplify the fluidodynamics project, helping the particles to flow into the channel, thanks to the buoyancy force. In that case either a capacitive or a resistive measurement could be possible.

Anyway, this kind of impedance sensing, e.g. for cell counting, is widely performed in liquid, while air microfluidics is not so common; a device being able to directly work in the air would be a greater accomplishment, besides the compactness and easier integrability discussed above. For these main reasons, all the efforts have been devoted to operate with air, thus sensing a capacitive variation.

The parallel-plate sensor has a main restriction: since one of the final goals is to classify PM particles according to their diameter, the gap between the two plates must be large enough to let even the bigger[1] mote pass through. A certain margin has to be taken into account, since PM is not actually composed by spheric objects, so a 30 μm gap may be enough to prevent the channel from clogging. Now, if the same sensor were used for every different diameters, the smaller[2] particles would probably determine a negligible perturbation of the sensing volume, being two orders of magnitude below the gap between the elec-

[1] 10 μm diameter
[2] 300 nm

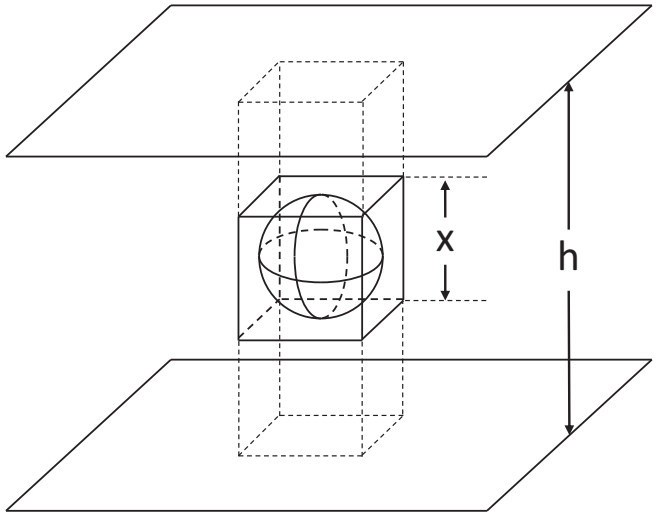

Figure 2.1: Estimation of the capacitance variation of a parallel-plate sensor; an equivalent circumscribed cube has been used to obtain an analytical expression for the capacitive signal.

trodes. Anyway, a quantitative analysis is necessary to come to such a conclusion. Nevertheless, this alternative provides a constant electric field, meaning a current signal independent of the particle position.

Let's now consider the coplanar case. The electric field is now less predictable, though a qualitative insight can be grasped. The field lines would eventually arrange in a circular fashion, being likely denser at the inner edges of the electrodes. The field intensity now depends on the position of the particle, so a source of uncertainty is added. The most sensitive area might just be the inner edges of the electrodes, so it could be advisable to locate the particles as close as possible to the gap; a proper focusing air flow would drive the particle to the desired position. Again, a quantitative analysis must be carried out.

2.2 Parallel-plate sensor

An analytical expression for the capacitive variation, although approximated, may be obtained by simple volume considerations, at least for the parallel-plate geometry. In this case, the expression of the capacitance is well-known: $C = A\epsilon_r\epsilon_0/d$, where A is the area of the plates, d is the gap between them, $\epsilon_r\epsilon_0$ is the absolute permittivity of the dielectric medium. The PM particle is replaced by a sphere with diameter equal to the aerodynamic equivalent diameter of the particle (see figure 2.1).

At first, let's consider the cube circumscribed to the sphere, having two faces parallel to the capacitor's plates, and the same dielectric constant as the sphere. This cube is contained into a parallelepipedon, where the capacitive variation takes place; the outer volume is a constant capacitance in parallel with it.

The parallelepipedon can be seen as the series of two parallel-plates capaci-

tors: the cube itself, and the air gap. Its capacitance, C_p, is equal to:

$$C_p = \frac{C_{cube}C_{air}}{C_{cube}+C_{air}} = \frac{x^2\epsilon_r\epsilon_0}{h\epsilon_r + x(1-\epsilon_r)}$$

being

$$C_{cube} = \frac{x^2\epsilon_r\epsilon_0}{x}$$

$$C_{air} = \frac{x^2\epsilon_0}{h-x}$$

leading to this variation:

$$\Delta C = \frac{x^2\epsilon_r\epsilon_0}{h\epsilon_r + x(1-\epsilon_r)} - \frac{x^2\epsilon_0}{h} = \frac{x^3\epsilon_0(\epsilon_r-1)}{h^2\epsilon_r + hx(1-\epsilon_r)}$$

For small x values, i.e. for particles much less than the channel size, we see that:

$$\Delta C \longrightarrow \frac{x^3\epsilon_0(\epsilon_r-1)}{h^2\epsilon_r}$$

This formula can be rearranged in a way easier to be remembered, which also highlights some important features:

$$\Delta C \longrightarrow \frac{\epsilon_0}{h}x^2\frac{x^3}{hx^2}\frac{\epsilon_r-1}{\epsilon_r} = C_p\frac{V_{cube}}{V_p}\frac{\Delta\epsilon_r}{\epsilon_r} \tag{2.1}$$

Now we can see that if a volume equal to V_{cube} changes its permittivity, it produces a capacitive variation which is a fraction of the total capacitance, according to the relative volume V_{cube}/V_p and to the relative permittivity variation; this last term is always less than 1, to which it tends if $\epsilon_r \to \infty$. This is reasonable: by increasing ϵ_r until the particle's capacitance becomes much greater than C_{air}, this last term becomes the significant one in the series of the two, and any further increase in C_{cube} is meaningless.

If we now consider the spherical particle, two analogue expressions can be constructed for the general and the approximated cases, respectively; the cube's volume and side are simply replaced by the sphere's volume and radius:

$$\Delta C \simeq 4/3\pi R^3\frac{\epsilon_0(\epsilon_r-1)}{h^2\epsilon_r + hR(1-\epsilon_r)} \tag{2.2}$$

$$\Delta C \longrightarrow 4/3\pi R^3\frac{\epsilon_0(\epsilon_r-1)}{h^2\epsilon_r} \tag{2.3}$$

To have an idea of how intense the capacitive signal could be, let's consider plastic spheres, having $\epsilon_r = 2$, which is a reasonable value for a consistent fraction of PM [2], as a function of the diameter. The gap between the plates has been chosen equal to 30 µm, since it must allow at least PM_{10} to flow. Such a margin has been taken because real particles are not spherical at all, so one must be careful to avoid the clogging of the channel.

Figure 2.2a is a log-log plot of the capacitive variation, according to equation (2.2). The slope is 60 dB per decade, clearly proving that the signal is proportional to the particle's volume, as in equation (2.3).

Regarding PM_{10}, we therefore expect $\Delta C \approx 3$ aF, an easily achievable sensitivity for most of the electronic instrumentations [11]. When dealing with $PM_{2.5}$, things drastically change: for a 1 µm particle the signal has decreased to 3 zF,[3] a very difficult value to measure even for an integrated system [12].

This geometry doesn't seem to be suited to detect $PM_{2.5}$. One could object that this is a consquence of the channel sizing, in order to measure all the different diameters together. If the particles were previously sorted, the finer fraction might be sensed by a customized sensor, e.g., with a 3 µm gap (see figure 2.2b). In that case, the variation would rise back to more than 3 aF, making it a very promising solution. However, there are some major drawbacks, mainly due to technological issues. This geometry would require a non standard fabrication process, which so far is not available. Secondly, the fractioning stage would rise the complexity of the microfluidic design.

In conclusion, this geometry has the potentiality to detect the particles within the desired diameter range, but, for the reasons listed above, the coplanar geometry will be now investigated.

2.3 Coplanar electrodes sensor

2.3.1 Coarse estimation

A couple of coplanar plane electrodes is shown in figure 2.3: they act as a capacitor. The electric field lines have been traced in a qualitative way. These electrodes can be easily fabricated over a glass substrate, by means of a lithographic process. Then, a microfluidic channel is placed on this surface; a molded lid made of Polydimethylsiloxane (PDMS) is generally used for the purpose. An air flow containing PM particles flows into this channel. Since the electric field is supposed to be more intense at the surface, near the gap between the electrodes, the particles should flow as close as possible to that position; a secondary air flow, orthogonal to the surface, may force the particles to this condition.

It is now clear the main advantage of this geometry: a single couple of electrodes could be used to sense particles of different size, if the air flow were conveyed as explained above. In case different parameter choices were more suited for different particle diameters, an array of optimized electrodes could be realized as well.

The expected capacitive variation, is, however, much more complex to determine, due to the non homogeneous electric field distribution. The conformal mapping method allows to derive an expression for the capacitance per unit length of two coplanar electrodes, as shown in Chen *et al.* [13]:

$$C = 2\epsilon_0 \frac{\epsilon_{r1} + \epsilon_{r2}}{2\pi} \ln\left[\left(1 + \frac{2L}{G}\right) + \sqrt{\left(1 + \frac{2L}{G}\right)^2 - 1}\right] W \tag{2.4}$$

[3] Now the diameter is reduced by a factor of ten; the signal scales with the volume, a ten to the cube factor.

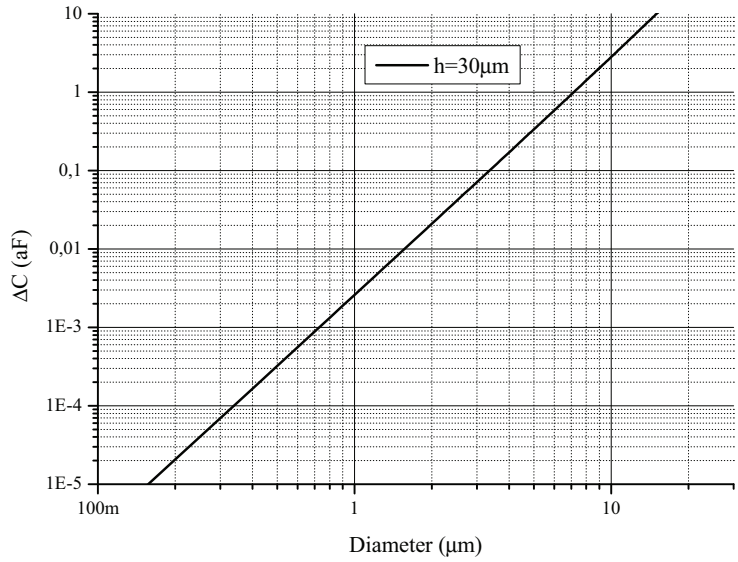

(a) *h=30µm.*

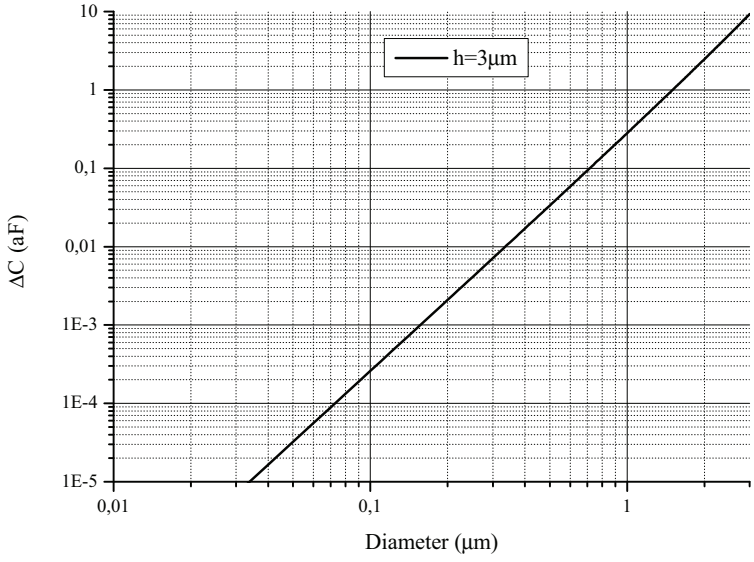

(b) *h=3µm.*

Figure 2.2: Log plot of the capacitance variation, using the general formula; the slope is practically 60 dB per decade, i.e. the variation is proportional to the particle's volume.

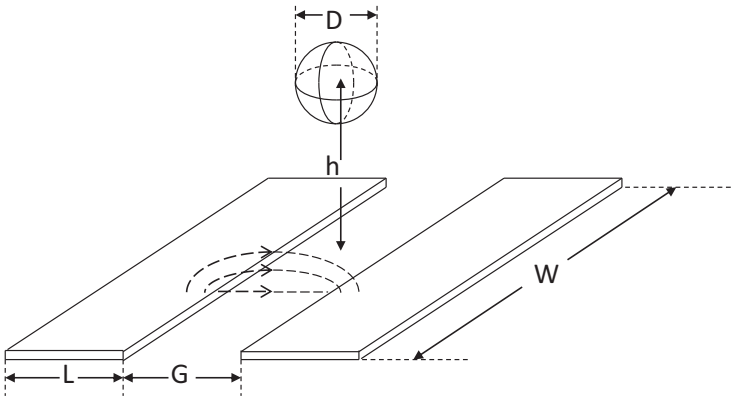

Figure 2.3: A couple of coplanar electrodes with their geometric parameters.

where G is the gap between the electrodes, L is their longitudinal width, W is their transversal width, ϵ_{r1} and ϵ_{r2} are the relative permeabilities of the half-spaces separated by the electrodes; the glass substrate has $\epsilon_r = 4.6$, while the upper half-space is filled with air.

For a pair of electrodes having $G = 10\,\mu\text{m}$ and $L = 20\,\text{um}$, this is equal to $36\,\text{aF}\,\mu\text{m}^{-1}$. If the electrodes were $100\,\mu\text{m}$ wide, the total capacitance would be 3.6 fF. By analogy with the parallel-plate geometry, the capacitive variation should be proportional to the particle's volume over the total capacitance volume, which resembles a cylinder of radius $L + G/2 = 25\,\mu\text{m}$ and height $W = 100\,\mu\text{m}$. Since the medium is half air and half glass, it is convenient to consider only the upper half of the cylinder, weighting it by $1/(1+\epsilon_r) \approx 0.18$ (if it were all air, it would be correctly equal to $1/2$). The signal due to a plastic sphere ($\epsilon_r \approx 2$) can be estimated as already done for the parallel-plate case, applying equation (2.1):

$$\Delta C \approx C_{total}\frac{V_{sphere}}{V_{total}}\frac{\Delta\epsilon_r}{\epsilon_r} = 3.6\,\text{fF}\frac{1}{1+\epsilon_r}\frac{4/3\pi R^3}{\pi(L+G/2)^2 W/2}\frac{\Delta\epsilon_r}{\epsilon_r} = 1.7\,\text{aF}$$

The result is encouraging, but this is of course a quite naive way to proceed. The conformal mapping method cannot be used to compute the capacitance in presence of a particle, therefore another approach is necessary to estimate with more accuracy the corresponding capacitive variation. A Finite Elements Method (FEM) simulation will be carried out in COMSOL Multiphysics; the value from the conformal mapping approach will serve as a cross check for the capacitance of the mere sensor.

2.3.2 Finite elements simulations

A series of 3D time-harmonic simulations with COMSOL Multiphysics have been performed, in order to estimate the capacitive signal for the coplanar geometry. Before exploring in depth every possible configuration for the electrodes, the signal order of magnitude is derived for a generic coplanar electrodes arrangement;

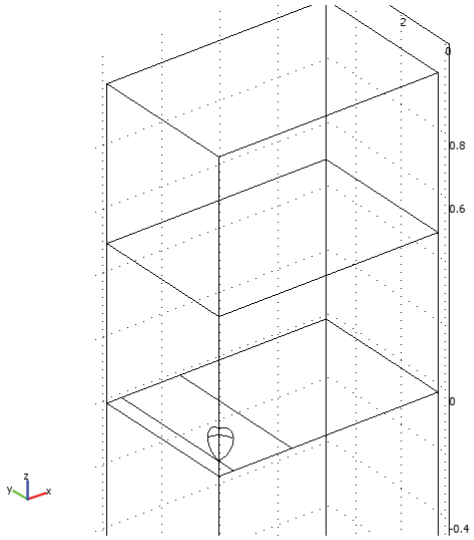

Figure 2.4: Simulation domain; two symmetry planes have been exploited.

the following example will show the approach adopted in all the other simulations. The dependence from the parameters involved will be studied later.

With reference to figure 2.3, a 10 µm diameter (D) sphere, with its center at 10 µm above the surface, has been placed between two coplanar electrodes. It seems reasonable to keep the sphere at such a distance from the pair, since a smaller value may cause the particle to hit them; moreover, the channel extends for 50 µm in height, that limits the vertical position of the sphere. The electrodes are separated by a 10 µm gap (G), while their longitudinal width (L) is 20 µm; such values match the diameter, for the electric field is expected to be properly perturbed in this configuration. The y-direction width (W) is much grater than L, since it must accommodate the microfluidic channel: a value of 1 mm is reasonable.

The physical domain implemented by the simulator is shown in figure 2.4. Actually, the overall volume of figure 2.3 has been divided in four parts, in order to exploit two symmetry planes; only a quarter volume is considered in the simulations, thus saving in computation. Therefore, only one half of electrode is visible, as well as a quarter of sphere. The electrodes have been truncated to 100 µm (only a 50 µm half electrode is visible), which is likely wide enough to include all the perturbation due to a 10 µm particle. The remaining part of them is a parallel constant capacitance which produces no signal. The technological process employed limits the thickness of the electrodes to about 200 nm, which has been neglected in the simulation domain.

Boundary conditions have to be chosen properly. Let's consider the whole volume, as in fig. 2.3. One electrode is stimulated by a sinusoidal voltage source, while the other one will be connected to the virtual ground of the transimpedance amplifier. The two electrodes have both a common mode and a differential mode voltage applied. The common mode voltage induces no cur-

Sub-domain	ϵ_r
GLASS	4.6
PDMS	2.75
AIR	1
SPHERE	2

Table 2.1: Subdomains permittivities.

rent into the sensor, therefore only the differential mode matters in order to calculate the capacitance of the sensor. We could reach the same result by applying a pure differential voltage between the electrodes: half of the voltage at one electrode, and the same half but with opposite sign at the other one. Now the electrostatic potential has an odd symmetry with respect to the y-z plane that crosses the origin[4], which must be at zero Volts. By forcing this plane to a ground boundary condition, we can simply forget the negative-x half-space, and compute the overall capacitance by halving the capacitance seen by the remaining electrode towards ground; this capacitance can be easily obtained by the admittance matrix returned by the program.

Now, let's consider the x-z plane: the electrostatic potential has an even symmetry with respect to this plane, i.e. no displacement current flows through it. So, nothing change if we split the remaining electrode by forcing an electrical isolation boundary condition at this plane. Again, we can forget the negative-y half-space, and compute the overall capacitance by doubling the capacitance seen by the remaining electrode towards ground.

To summarize, if both the conditions are applied, the total capacitance is equal to the one corresponding to that quarter of space. All the other external boundaries have been set to electrical isolation, and the internal ones to the continuity of two dielectric regions, except for the half-electrode area, which has been set to a port with forced voltage.

All the geometric sub-volumes are dielectrics; their permittivities have been chosen as in table 2.1. The simulation domain is the same for both the case with the sphere and without it; one can shift from the former to the latter by simply changing the permittivity of the quarter-of-sphere subdomain, from 1 (no sphere) to 2 (sphere with $\epsilon_r = 2$). The main reason for this operating choice is that it keeps the same FEM mesh; if not, the capacitance variation would be mainly due to the mesh change, that would have absolutely no sense.

The simulator returned 3.871 951 fF for the initial capacitance (very close to the conformal mapping value), and a variation of 2.397 aF. This last value is of the same order of magnitude of the one estimated in section 2.3.1, but undoubtedly more reliable. This result suggests that coplanar sensors have signal performances similar to parallel-plate sensors; however, this has been verified only for the 10 µm particle, with a quite arbitrary choice of the parameters involved. Hence, many other different situations must be simulated, in order to understand how these parameters affect the signal, and how to use this information for the design of the optimum sensor.

[4]Same reference system of fig. 2.4.

Name	Description
D	Particle's diameter
G	Gap between the electrodes
L	Electrode's length
W	Electrode's width
h	Distance of the particle's center from the surface
ϵ_r	Particle's dielectric permittivity

Table 2.2: Coplanar electrodes parameters.

Fixed parameters		G	C_0	C	ΔC
Name	Value	(μm)	(fF)	(fF)	(aF)
D (μm)	10	20	3.164 569	3.165 938	1.369
L (μm)	20	15	3.446 417	3.448 230	1.813
W (μm)	100	10	3.980 185	3.982 602	2.417
h (μm)	10	6	4.513 067	4.515 964	2.897
ϵ_r	2	4	5.142 898	5.145 987	3.089
		2	6.193 249	6.196 461	3.212
		1	7.216 955	7.220 184	3.229

Table 2.3: Capacitive variation as a function of the gap G.

2.3.3 Parameters dependences

The main parameters involved have been introduced in the previous subsection, and they are listed in table 2.2. The signal's dependence from each of them will be studied, keeping the other ones constant. The computing approach is the same as in the first case-study.

Let's start with the gap G. The results of the simulations are summed up in table 2.3. On the left side the constant parameters have been listed; on the right side, next to each gap value, the sensor initial capacitance (C_0), the capacitance perturbed by the sphere (C), and the corresponding variation (ΔC) are shown.

As we could expect, the total capacitance increases by reducing the gap, similarly to a parallel-plate capacitor. In fact, if the gap is reduced, a grater electric field is necessary to maintain the same voltage[5] between the electrodes, therefore more charge has to be placed on them, thus increasing the capacitance. The capacitive variation also increases by reducing the gap, which might be the very first guideline for the sensor project.

The next parameter to be studied is the relative permittivity ϵ_r. Table 2.4 shows, as predictable, a capacitance gradually increasing with the permittivity; this increase is not, however, indefinite; following the analysis of section 2.2 as the particle's capacitance becomes dominant with respect to the air capacitance, the series is approximated only by the smaller one, without being affected by further changes of the permittivity. This has already been highlighted in equation (2.1), and figure 2.6 clearly depicts this trend.

[5] $\Delta V_{AB} = -\int_B^A \vec{E}\,\vec{dl}$

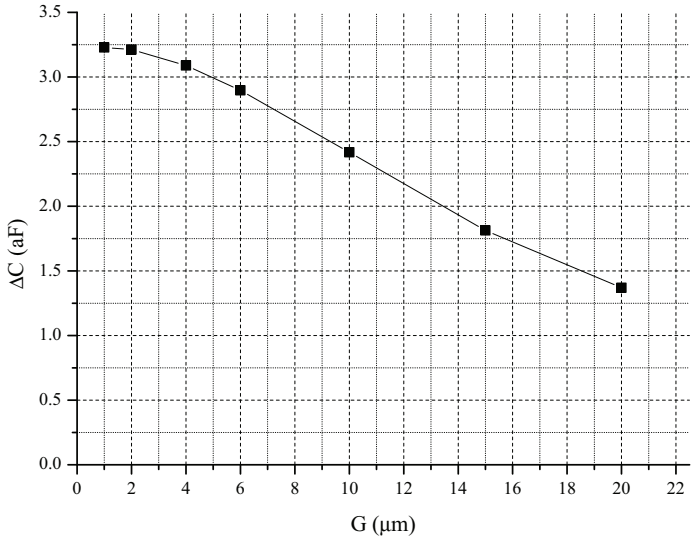

Figure 2.5: Capacitive variation as a function of the gap G.

Fixed parameters		ϵ_r	C	ΔC	ϵ_r	C	ΔC
Name	Value		(fF)	(aF)		(fF)	(aF)
D (μm)	10	1	3.761 525	0.000	20	3.769 826	8.301
L (μm)	20	2	3.763 920	2.395	30	3.770 238	8.713
W (μm)	100	3	3.765 359	3.834	40	3.770 454	8.929
h (μm)	10	4	3.766 320	4.795	50	3.770 587	9.062
G (μm)	2	5	3.767 008	5.483	60	3.770 677	9.152
		6	3.767 523	5.998	70	3.770 742	9.217
		7	3.767 925	6.400	80	3.770 791	9.266
		8	3.768 246	6.721	90	3.770 830	9.305
		9	3.768 509	6.984	100	3.770 861	9.336
		10	3.768 728	7.203	1000	3.771 116	9.591

Table 2.4: Capacitive variation as a function of the relative permittivity ϵ_r.

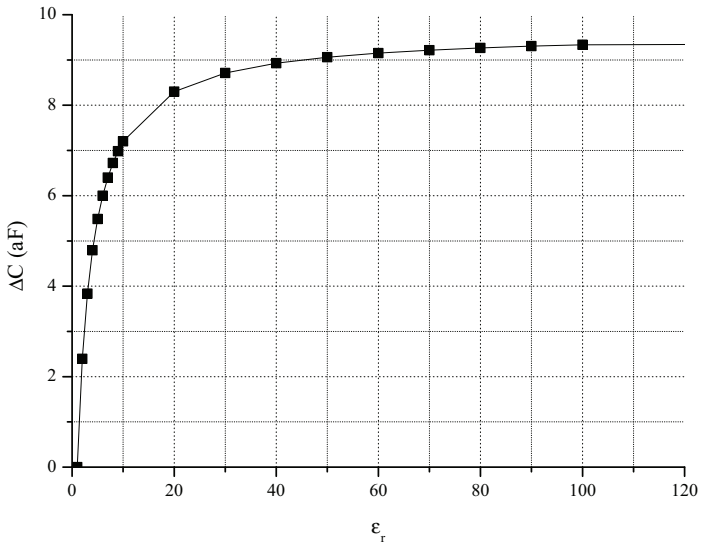

Figure 2.6: Capacitive variation as a function of the relative permittivity ϵ_r.

The permittivity is strictly linked to the material whom the particle is made of, therefore the consequences on PM detection are twofold. For a given diameter, different permittivities lead to different signal levels; the resulting detector would be able to distinguish and sort the particles according to their material, which is quite an accomplishment. On the other hand, this would imply to have already sorted PM in diameter classes, but this is just the detector's job. The primary goals are to detect PM and to measure its diameter through an impedance measurement, so the variability due to the permittivity looks more like a drawback, rather than a valuable feature. Let's consider figure 2.6: a 10 µm particle with $\epsilon_r = 2$ would lead to a 2.4 aF signal; a similar particle with $\epsilon_r = 3$ gives 3.8 aF, so the corresponding variation is 1.4 aF. The same variation could be produced by a change in the particle's diameter, therefore it could be misinterpreted; a valid criterion must be developed in order to correctly interpret the capacitive information.

Anyway, for large permittivity values, the capacitive signal saturates at about 10 aF. For $\epsilon_r > 15$ the variation is fairly negligible when transduced into diameter uncertainty, considering that the geometrical dependence is much heavier (to the particle's volume).

At this point, the diameter dependence must be faced. The simulations results are listed in table 2.5. The FEM domain is now a bit different. A series of concentric spheres, one per diameter value, has been used instead of a single sphere. When considering a certain diameter value, one must simply set the correct value for the spherical shells. This is the reason for the initial capacitance C_0 remains constant, being the mesh unchanged for each simulation.

The dependence on the permittivity has also been taken into account: the diameter varies while $\epsilon_r = 2$ or $\epsilon_r = 15$. As expected, the signal is greater

Fixed parameters		D	C	ΔC
Name	Value	(μm)	(fF)	(aF)
G (μm)	2	0.3	7.122 229	0.000
L (μm)	40	1	7.122 230	0.001
W (μm)	100	2	7.122 255	0.026
h (μm)	10	4	7.122 441	0.212
ϵ_r	2	6	7.122 960	0.731
		8	7.124 019	1.790
C_0 (fF)	7.122229	10	7.125 893	3.664
		15	7.137 323	15.094

(a) $\epsilon_r = 2$.

Fixed parameters		D	C	ΔC
Name	Value	(μm)	(fF)	(aF)
G (μm)	2	0.3	7.122 230	0.001
L (μm)	40	1	7.122 240	0.011
W (μm)	100	2	7.122 315	0.086
h (μm)	10	4	7.122 925	0.696
ϵ_r	15	6	7.124 632	2.403
		8	7.128 117	5.888
C_0 (fF)	7.122229	10	7.134 293	12.064
		15	7.173 056	50.827

(b) $\epsilon_r = 15$.

Table 2.5: Capacitive variation as a function of the diameter D.

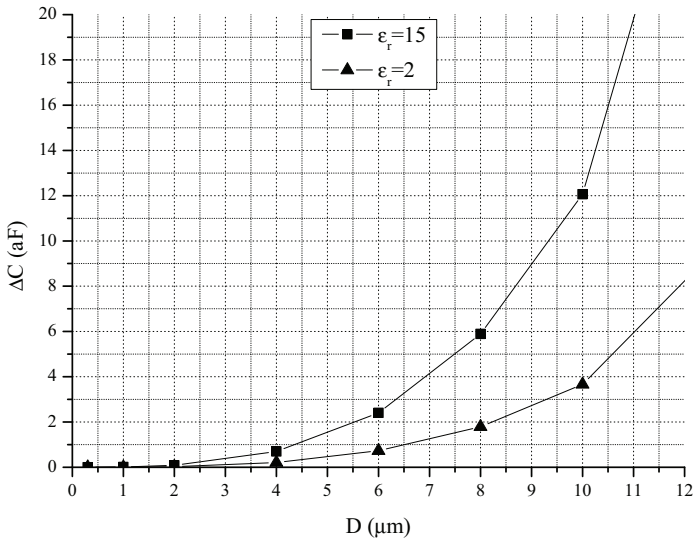

Figure 2.7: Capacitive variation as a function of the diameter D.

for $\epsilon_r = 15$ when the diameter is the same. The most important result from this analysis is, however, the strong dependence of the signal by the particle's volume. From tables 2.5a and 2.5b one can verify that by halving the diameter, the capacitive variation scales by a factor of 8, and so on. This dependence cannot be taken as a stern general rule, the electric field not being constant. It worked pretty well for these particular situations, and we might explain it by observing that the diameter was changed 'in the proper way'. Let's consider the 5 μm sphere; the electric field is stronger below it, and weaker above it (it will be verified in the next lines). By doubling the diameter while keeping the same distance h, the new volume extends itself both above and below, thus keeping the same average electric field, more or less.

In the worst scenario, i.e. for $\epsilon_r = 2$, detecting a 8 μm might be very difficult, looking at the values predicted by the FEM. Greater values are expected if the particle gets closer to the surface, so the next parameter under investigation is the distance h, that is the distance of the sphere's center from the surface. Table 2.6 and figure 2.8 show the results, that indicate an increase in capacitive signal as the sphere gets closer to the surface, according to the picture of a more intense electric field in the gap region. It would be desirable to keep the particles at the minimum possible distance, to maximize the signal.

If we concentrate on the horizontal flow model, we must keep a minimum distance to let the particles flow; moreover, if all the PM is intended to be measured in a single air flow, the smaller particles have to remain into the same layer of air that also carries the bigger particles; these are the ones which determine the minimum value for the distance h, which may be inadequate for measuring the smaller ones.

A totally different measurement approach may overcome this issue: instead

Fixed parameters		h	C_0	C	ΔC
Name	Value	(µm)	(fF)	(fF)	(aF)
D (µm)	10	5	3.930 502	3.937 515	7.013
G (µm)	10	6	3.870 561	3.876 004	5.443
L (µm)	20	7	3.920 827	3.925 245	4.418
W (µm)	100	8	3.942 593	3.946 190	3.597
ϵ_r	2	9	3.916 833	3.919 767	2.934
		10	3.887 811	3.890 231	2.420
		11	3.887 910	3.889 906	1.996
		12	3.727 595	3.729 237	1.642
		13	3.855 227	3.856 612	1.385
		14	3.878 345	3.879 522	1.177
		15	3.861 428	3.862 425	0.997
		20	3.764 488	3.764 955	0.467
		25	3.798 903	3.799 141	0.238
		30	3.806 880	3.807 010	0.130
		35	3.797 085	3.797 158	0.073

Table 2.6: Capacitive variation as a function of the distance h.

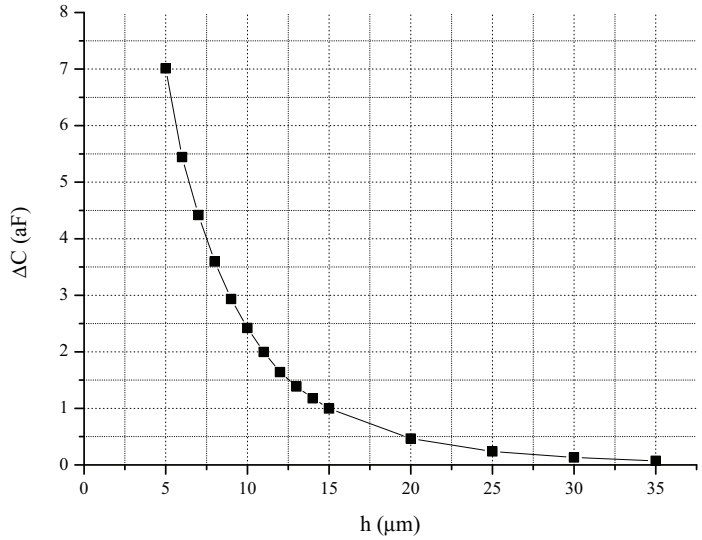

Figure 2.8: Capacitive variation as a function of the distance h.

Fixed parameters		L	C_0	C	ΔC
Name	Value	(μm)	(fF)	(fF)	(aF)
D (μm)	10	2	1.566503	1.567091	0.588
G (μm)	10	5	2.137153	2.138298	1.145
W (μm)	100	10	3.026394	3.028210	1.816
h (μm)	10	15	3.478472	3.480655	2.183
ϵ_r	2	20	3.761525	3.763920	2.395
		30	4.303638	4.306269	2.631
		40	4.711345	4.714041	2.696
		50	4.907003	4.909727	2.724
		100	5.924799	5.927615	2.816

Table 2.7: Capacitive variation as a function of the length L.

of making PM travel as close as possible to the surface in a laminar flow, the particles may drop on the electrodes from above, provided that they always reach a sensitive area with high probability.

The last parameter to analyze is the length L. It is difficult to find an analogue parameter for an equivalent parallel-plate capacitor, that may help to predict this dependence. In some way it is related to the plates area; if L increases, then the total capacitance is expected to increase, too, that has been well highlighted by equation 2.4. However, increasing L also produces a greater capacitance variation, that means a more intense electric field. Figure 2.10 shows the electric potential isosurfaces in the sensor region: it varies from 1 V (red) to 0 V (blue). The sensor's electric field (2.10a), being orthogonal to the isosurfaces, comes out of the plate in a quite circular fashion, except for the gap region, where it goes directly towards the other electrode. The electric field arrangement resembles the one generated by a punctiform charge dipole, but in this case the two 'charges' are the coplanar plates. A sphere with $\epsilon_r = 10$ (2.10b) perturbs the electric field: the isosurfaces bend, and they are now less dense into the sphere's volume, where the electric field becomes less intense. It is desirable that the initial electric field perturbed by the sphere is as intense as possible, i.e. the isosurfaces have to be dense. Figures 2.10c and 2.10d show a close-up comparison between sensors having L=20 μm and L=50 μm. In the latter case there more isosurfaces are going to be intercepted by the sphere, so their gradient is greater, meaning a more intense electric field, thus producing a more intense capacitive variation.

In conclusion, the length L should be maximized to get the highest signal. This improvement is not, however, infinite, as depicted in figure 2.9. At some point (30 μm for this particular situation) the capacitance rises much more slowly, being any further increase in L totally useless. One must also remember that L makes also the total capacitance grow up, which may represent a drawback (it adds more parasitics to the processing stage, for example).

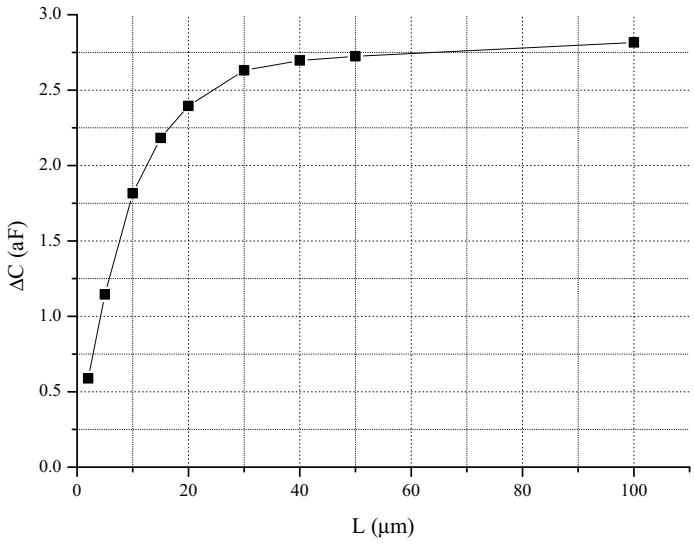

Figure 2.9: Capacitive variation as a function of the length L.

2.4 Oblique electrodes

The parametric simulations have shown a quite predictable result: in order to maximize the capacitive variation, one must increase the electric field perturbed by the particles; this has been accomplished, for example, by reducing the gap between the electrodes. To increase the electric field, for a given voltage between the electrodes, means 'to compress' the isosurfaces of the electric potential, at least around the gap region, which is the most sensitive one. If the electrodes could lean in an oblique position, but still allowing the particles to flow between them, there might be some improvement. This idea is halfway between the coplanar and the parallel-plates geometries, and is shown on figure 2.11. Such a pair of electrodes, at about 45° with respect to the surface, can be actually realized by the technological process employed**inserire riferimento tecnologia**, but the cost is higher; one must analyze this geometry, and see if the improvements justify the greater cost.

Table 2.8 summarizes the results. The parameters have exactly the same meaning for both geometries, and they have already been defined previously. The one not shown are the distance from the surface h (10 μm), the electrodes' length L (30 μm), and width (100 μm). We see that the corresponding capacitive variation is greater for the oblique geometry of a factor of two, more or less. Although this arrangement leads to an improvement, it is not worth the risk: the 10 μm particle produces a signal which is already detectable by the current instrumentations. Doubling the signal is quite an accomplishment, but it does not justify the employment of a more complex technological process, nor the increased complexity of the fluidodynamic project, at least at such a preliminary design stage.

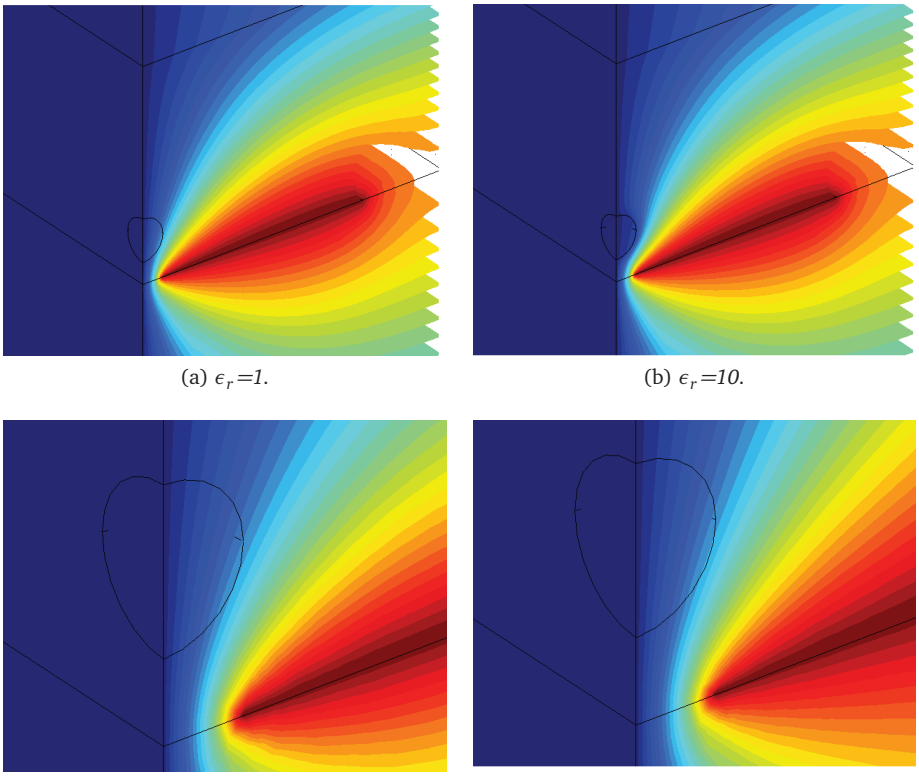

(a) ϵ_r=1. (b) ϵ_r=10.

(c) L=20 µm. (d) L=50 µm.

Figure 2.10: Electric potential isosurfaces in the sensor region.

D (µm)	G (µm)	ϵ_r	C_0 (fF)	C (fF)	ΔC (aF)
10	10	2	4.413 687	4.416 305	2.618
10	10	15	4.413 687	4.422 346	8.659
2	2	2	6.717 573	6.717 597	0.024
2	2	15	6.717 573	6.717 653	0.080

(a) *Coplanar electrodes.*

D (µm)	G (µm)	ϵ_r	C_0 (fF)	C (fF)	ΔC (aF)
10	10	2	7.416 966	7.421 686	4.720
10	10	15	7.416 966	7.432 775	15.809
2	2	2	10.888 022	10.888 085	0.063
2	2	15	10.888 022	10.888 229	0.207

(b) *Oblique electrodes.*

Table 2.8: Comparison between coplanar and oblique electrodes.

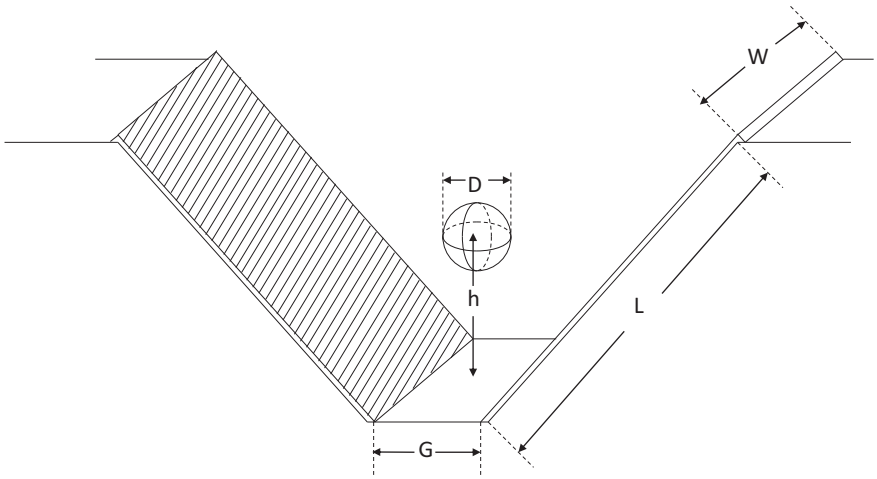

Figure 2.11: A couple of oblique electrodes and their geometric parameters.

2.5 Pulse shape

The signal produced by the sensor depends on the way it is operated. If the particulate drops on the sensor in a sensitive area, the capacitance varies as a step function, with a slope related to the falling speed of the particles. Conversely, if they flow above the electrodes, the capacitance varies only for a brief time interval, which is related to the particle's speed. It could be interesting to study this pulse shape depending on the particle's diameter: if different diameters produce different shapes, this property would give a criterion to sort them in size classes even if there is a variability of permittivity. The pulse shapes produced by a set of spherical beads, with the same permittivity and different diameters, would be measured and stored. Instead of a standard low pass filter, the lock in amplifier could perform a synchronous filtering, testing all the stored pulse shapes in parallel; the one that matches the particle's unknown diameter produces the highest value, and is the optimum filter. Once the diameter is identified, the pulse height would depend only on the particle's permittivity. This approach needs more filtering stages in parallel to be done in digital domain, so the required FPGA performances would be more severe. Furthermore, we are assuming the pulse shape not to be dependent on the permittivity.

The pulse shape has been estimated by moving the sphere along the channel, and then measuring the static capacitive variation for each position. This time, only one symmetry plane has been exploited, therefore the usual geometric domain had to be changed accordingly. This has been done for two spheres having

Fixed parameters		x	C_0	C	ΔC	ΔC_{NORM}
Name	Value	(μm)	(fF)	(fF)	(aF)	(m^{-1})
D (μm)	2.5	0	2.516 814	2.516 882	0.136	80 188.7
G (μm)	4	2	2.493 333	2.493 401	0.136	80 188.7
W (μm)	100	4	2.498 860	2.498 925	0.130	76 651.0
h (μm)	10	6	2.499 426	2.499 484	0.116	68 396.2
ϵ_r	15	8	2.494 570	2.494 621	0.102	60 141.5
L (μm)	20	10	2.489 407	2.489 451	0.088	51 886.8
Area (aF μm)	1.696	12	2.468 798	2.468 835	0.074	43 632.1
		14	2.491 210	2.491 243	0.066	38 915.1

(a) D=2.5 μm

Fixed parameters		x	C_0	C	ΔC	ΔC_{NORM}
Name	Value	(μm)	(fF)	(fF)	(aF)	(m^{-1})
D (μm)	10	0	2.516 814	2.521 872	10.116	81 451.9
G (μm)	4	2	2.493 333	2.498 381	10.096	80 188.7
W (μm)	100	4	2.498 860	2.503 595	9.470	76 250.4
h (μm)	10	6	2.499 426	2.503 671	8.490	68 359.7
ϵ_r	15	8	2.494 570	2.498 257	7.374	59 373.9
L (μm)	20	10	2.489 407	2.492 596	6.378	51 354.3
Area (aF μm)	124	12	2.468 798	2.471 531	5.466	44 011.1
		14	2.491 210	2.493 564	4.708	37 907.8

(b) D=10 μm

Table 2.9: Derivation of the pulse shape from static capacitive variations, for a sphere having $\epsilon_r = 15$.

$\epsilon_r = 15$ and diameters of 2.5 μm and 10 μm (see figure 2.12 and table 2.9).

The pulse shapes have been normalized to their respective areas, so that they have unitary area, for a fair shape comparison. The results show that there is actually no difference between them, thus ruling out the optimum filter approach for distinguishing diameter variations from permittivity variations. Nevertheless, the particles could be separated according to their diameter before being sensed, by exploiting microfluidodynamic properties; this has already been accomplished by [14], who separated particulate matter by size directly in the air.

This analysis provides with some information on the pulse time duration, which is related to the signal's bandwidth, and dictates some specifications for the system. Looking at the figure, the pulse is produced on a spatial range of the order of 10 μm around the gap. This means that if the particles travels at 1 mm/s, the pulse lasts 10 ms, so its bandwidth is 100 Hz; the system's bandwidth after lock-in operation determines the system's noise and the minimum detectable amplitude, so it can be set to the same value, or a decade beyond. One may set the minimum particle's speed for fluidodynamic issues, and then obtain the minimum lock-in bandwidth; or, which is indeed the case, one can set the maximum lock-in bandwidth for a given sensitivity, which automatically fixes the maximum particle's speed. In order to reach such a sensitivity (1 aF),

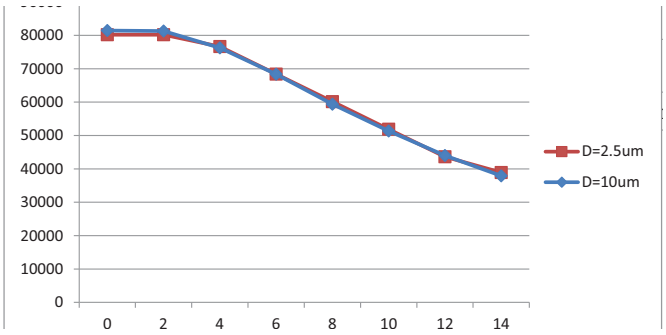

Figure 2.12: Comparison between the pulse shapes produced by two spheres with different diameters.

the lock-in amplifier cannot afford a bandwidth greater than 1 kHz, [11], so the particle's speed has to be limited to 10 mm/s.

This compromise is absent if we adopt the vertical fall approach, instead of the horizontal flow one: in that case, the particles drop at their regime speed, and the system can detect the low frequency changes of the capacitance's steady state value.

2.6 Theoretical sensitivity

In the previous sections some geometric configurations have been analyzed, aiming to find out the most suitable for a capacitive measurement in the air of particulate matter. The simulations have shown that the coplanar configuration is the best compromise between sensitivity and fabrication simplicity. It has been shown that this geometry should be able to detect a particle of 10 µm diameter, even for the lowest permittivity value, and with the particle flowing at a certain distance from them, i.e. PM_{10} should be well detectable. However, this detector is intended to measure also finer particles, so the sensitivity to the 1 µm diameter particle is now investigated. To do so, the particle has been placed in touch with the surface, being the most sensitive area; the gap has been minimized to the minimum available value of the technological process employed, i.e. 2 µm. The simulator returns 0.96 aF when $\epsilon_r = 15$, and 0.28 aF when $\epsilon_r = 2$. Only for high permittivity values we get close to the reference value of 1 aF.

May these signals not be enough for the detection, the measurement could be performed in water, instead. Water has been neglected so far, because it implies a more complex management system: somehow PM must be transferred from air into water, that may be possible, but it rises the complexity of the fluidodynamic project. Then, water impedance measurement have widely been performed because of the higher obtainable signal, so that would not be a satisfying result. If needed, a water measurement could be resistive or capacitive, depending on the water conductivity; typical values are 1 S/m for a saline compound behaving like a resistance, or zero for distilled water, which behaves like a capacitance. Water relative permittivity is about 80. The simulation results are listed in table 2.10.

Water measurements are clearly superior in terms of signal level: a 1 µm

ϵ_r	ΔC_{air} (aF)	ΔC_{water} (aF)	ΔR_{water} (Ω)	ΔG_{water} (nS)
2	0.28	-48	3	83
15	0.96	-37	3	83

Table 2.10: Size sensitivity comparison between air and water measurements.

particle could be well detectable either with a capacitive or a resistive measurement; the capacitive one gives variations (negative, since the permittivity in the sphere region lowers) of the order of tens of atto Farad; the resistive variations are even of the order of one Ohm. Although these promising performances, as already said, the water measure is not challenging, and it will be put aside; in case the air measurement won't give the expected results, water measurement will be the second-best solution.

2.7 Sensor layout

The sensors have been fabricated according to the coplanar geometry, following the horizontal flow approach. They are basically plane metal lines deposited on a glass substrate, consisting of an 8 inch glass wafer. The electrodes are made of gold, but there is also a thin (20 nm) adhesion layer made of titanium; the overall electrode's thickness is 200 nm. The wafer layout is shown on figure 2.14. The area has been divided into four main slides, named "A" "B" "C" and "D" starting from top, and into four little slides at the sides, all named E, since they are all equal.

The main slides differ for some parameter choices, but they all share the same structure (see fig 2.13). On the right side there is an array (named "d") of five couples of electrodes, numerated from 1 to 5 starting from left. These are the sensing electrodes that the particle flowing from left to right would encounter, thus producing a series of five pulses for a single travel, one per sensor (they have been sufficiently separated to avoid the superposition of different pulses). These sensors have one parameter varying, so that the traveling particle would produce different pulses; the aim is to validate the parameter dependences inferred from the previous simulations. Electrodes "Ad" have L=30 μm, but gap equal to 2, 4, 6, 10 and 20 μm from left to right, respectively. The lithographic resolution is about 2 μm, which dictates the minimum gap value, although the 4 μm one is expected to be more reliable in terms of unwanted short-circuits. Moreover, only on slide A, the electrodes with gap 4 and 10 μm are not couples, but triples with two gaps per each, in order to perform a differential measurement. The two outer electrodes will be driven by voltage sinusoids in phase opposition, and the inner one will sink the two currents produced, thus performing an intrinsic difference operation: if there is no particle, and everything is perfectly balanced, no net current is read by the processing stage; if the particle is flowing, it unbalances the sensor, and a bipolar current signal is produced. Electrodes "Bd" have all the same gap, equal to 4 μm, which maximizes the signal, but they have different length L; its values are 10, 20, 30, 60 and 100 μm. Electrodes 'Cd' are basically the same as "Ad", but there aren't any triples. Elec-

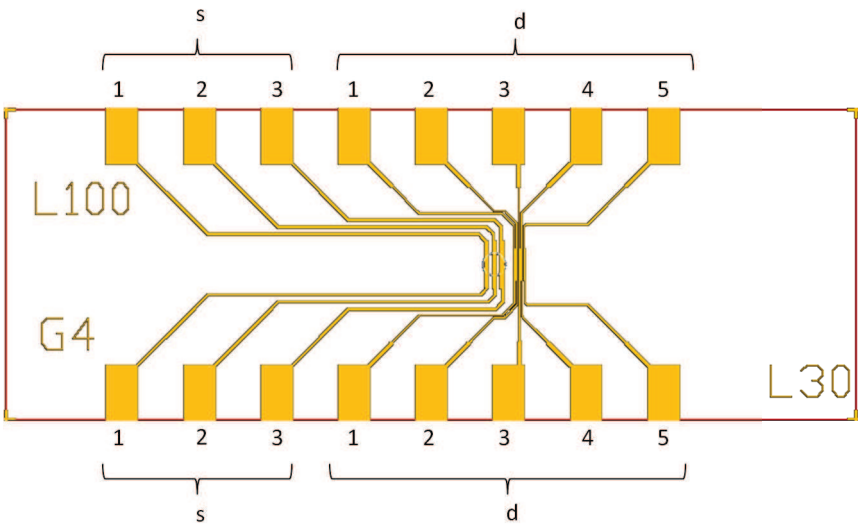

Figure 2.13: Close-up of a single rectangular slide; the the two groups "s" and "d" are indicated, as well as the single electrode's progressive numbers.

trodes 'Dd' are similar to 'Cd', but L has been set to 100 µm, in case the others would prove to be too much weak.

The width W has been chosen equal to 1.5 mm, since the air channel resulting from the PDMS mold is 500 µm wide, and it must be correctly aligned. Of course, the greater the width, the greater the overall sensor capacitance. In this case, the most critical value expected is around 200 fF, which is negligible with respect to the parasitics of the following discrete components circuit, that are likely of the order of some pico Farad.

Still on the main slides, on the left side there is a group of three sensors, named "s". These are related to the fluidodynamic project. One of the options to drive the air flows was the creation of a lower level circular region (well), preceding the sensing area, where the particles could be properly conditioned in order to reach the sensors at the desired speed and height. The group "s" should track the particles into the well, to validate the fluidodynamic project. Anyway, for the first manufacturing process there isn't any well, and the two groups have been simply fabricated on the same level. These 'well' electrodes have been then replicated on the "E" slides; they have a 4 µm gap, 100 µm length, and 3 mm width.

All the electrodes have been linked by metal traces to their respective outer pads, which are located at the upper and lower edges of the slide. The pads have been associated alternating the two edges, in order to avoid capacitive couplings between the two (or three) electrodes of the same sensor, trying to keep the upper and lower edges as symmetrical as possible. All the sensors on the main slides have been gathered in the middle, to leave room for the inlet and outlet paths on the left and right side.

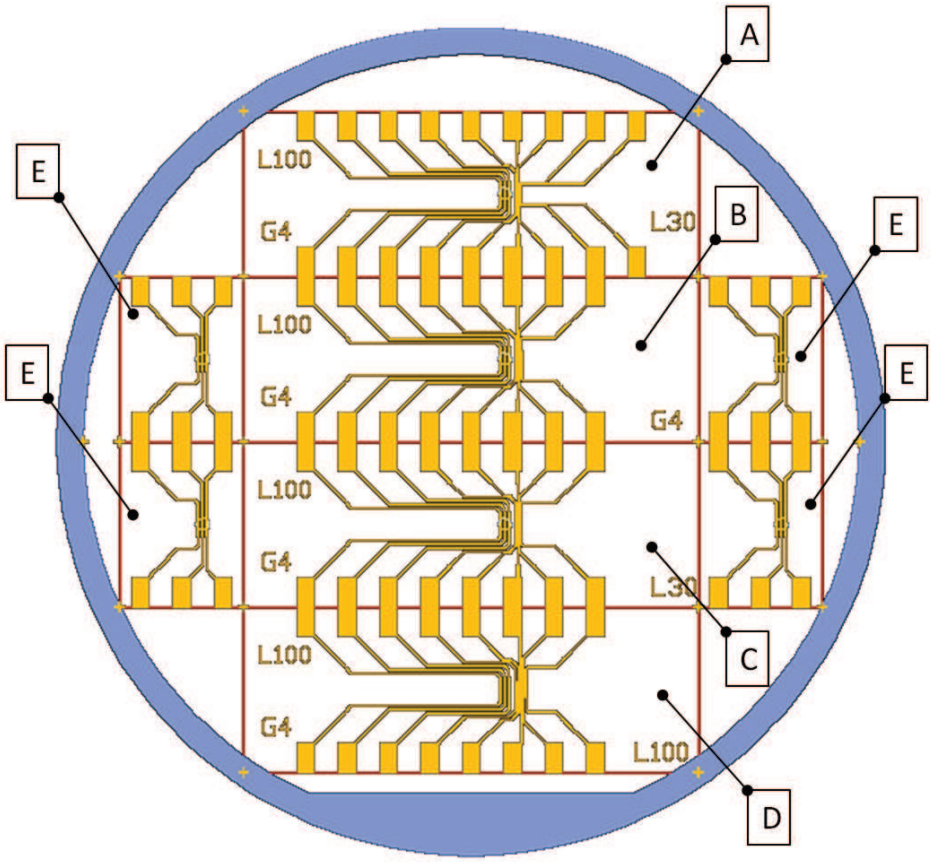

Figure 2.14: Whole wafer image: the capital letters indicate different slides.

Chapter 3

Analog front end design

3.1 Introduction

The capacitive sensor is stimulated by a sinusoidal voltage waveform, and it produces a phase quadrature sinusoidal current; when the particle perturbs the electrodes, causing the capacitance to vary in time, this current experiences a weak amplitude modulation,[1]; this is the signal that has to be detected by a lock in demodulation. The following processing stages work on voltage signals: a transimpedance amplifier is therefore necessary. It converts the capacitive current into a voltage waveform; moreover, it should desensitize the transduced signal from the noise of the following stages. When this condition is verified, only the preamplifier limits the minimum detectable current, that must be compared to the noise of the transimpedance itself, which is therefore one of the most critical parameters. As already discussed, in order to read capacitive variations of 1 aF, an equivalent noise bandwidth of 1 kHz will be considered.

The frequency of the sinusoidal reference also affects the signal-to-noise ratio. The 1/f noise corner frequency of an opamp can easily reach values such as 10 kHz, so the reference's frequency may be chosen between 100 kHz and 10 MHz; the upper limit is set by the time delays, which become significant at those frequencies. The modulated signal is then expected to have a narrow relative bandwidth around a certain frequency value, which must optimize the measurement sensitivity. The transimpedance is then required to work up to 10 MHz.

The simplest and most immediate topology for a transimpedance is certainly the OPAMP with feedback impedance, that reads the sensor's current from the virtual ground; this circuit is described in section 3.2. It has been adopted as a basic choice for the very first measurements. Afterwards, the employment of an inductor to improve the sensitivity is studied in section 3.5; finally, a higher resolution preamplifier has been designed, which is described in section 3.6.

The reading circuit also include an inverting buffer that provides the same reference, but with opposite sign, in order to perform a differential measurement. The advantage with this approach is twofold: the noise from the generator of the reference signal is reduced (ideally it should be canceled); the output

[1]The total capacitance of the sensor is of the order of 100 fF, while the signal is about 1 aF, so there are five orders of magnitude between them.

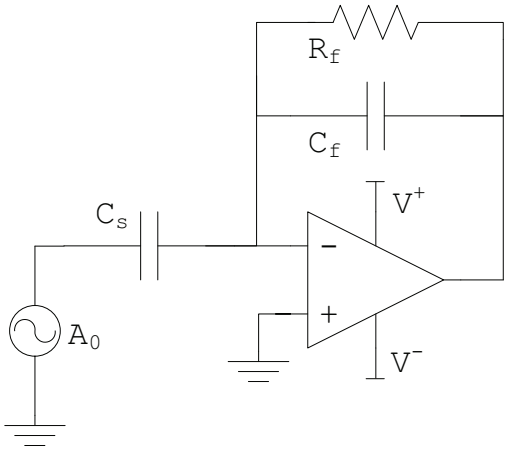

Figure 3.1: Very simple transimpedance amplifier attached to the capacitive sensor.

dynamic range specifications for the transimpedance amplifier are much less severe.

3.2 Integrator

3.2.1 Main features

Figure 3.1 shows the classic transimpedance amplifier with feedback impedance between the output node and the inverting input node. In this case, a capacitor was chosen as feedback impedance, so that the voltage gain between the output and the reference voltage sinusoid will not be frequency dependent, and it will be easily adjusted in order to satisfy the output voltage range; the current trasduction into voltage will be fixed, too; moreover, if a resistance had been placed, instead, it would have added its thermal noise, while a pure capacitance is noise free.

The feedback impedance is not actually purely capacitive: a resistor has been placed in parallel to C_f, in order to set the bias point. As mentioned before, this resistance adds its thermal noise, so the value must be chosen properly. A 1 GΩ resistance carries 4 fAHz$^{-1/2}$, which will be shown to be negligible with respect to other noise sources.

By applying a voltage sinusoidal input with amplitude A_0, the output node also swings sinusoidally, between $\pm A_0 C_s/C_f$. When a capacitive variation of the sensor C_f occurs, due to some PM flowing over the electrodes, a current signal is produced:

$$i_s = j\omega \Delta C A_0$$

This current is read by the transimpedance virtual ground, and then converted

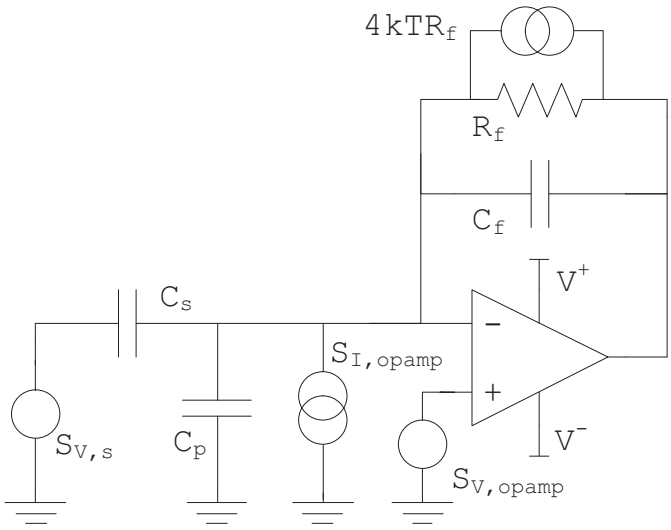

Figure 3.2: Same circuit, but noise sources have been highlighted.

into an output voltage signal:

$$v_{out} = \frac{\Delta C}{C_f} A_0$$

Of course, there is a minimum detectable signal: noise sources limit the system's resolution. Beside converting current into voltage, the transimpedance desensitizes the signal by the following stages' noise, which should be considered negligible. Under this assumption, noise analysis will be carried out by referring the signal-to-noise ratio (SNR) to the currents entering the virtual ground; both signal and noise are then amplified by the same amount by the feedback capacitor, thus keeping the SNR unchanged at the output node.

Three noise sources must be considered: the opamp, the feedback resistor, and the input voltage generator. The resistance's noise current has a spectral density equal to $4kT/R_f$, which is directly read by the virtual ground, as well as the current input equivalent noise of the opamp. The input generator noise follows the same transfer as the input reference signal, giving a current spectral density equal to $S_{V,gen}(\omega C_s)^2$. The voltage noise of the opamp is transferred at the output node by the noninverting gain:

$$S_{V,opamp}\left(1 + \frac{C_s + C_p}{C_f}\right)^2$$

which is equivalent to the following current at virtual ground:

$$S_{V,opamp}\omega^2(C_f + C_s + C_p)^2$$

The capacitor C_p represents both the input capacitance of the opamp and the

parasitic capacitance of the connections at the virtual ground node. These two noise sources are uncorrelated, hence their squared values are summed.

The SNR of the current entering the virtual ground can be then written this way: [2]

$$SNR = \frac{A_0 \omega \Delta C}{\sqrt{BW}\sqrt{S_{V,s}(\omega C_s)^2 + 4kT/R_f + S_{I,opamp} + S_{V,opamp}\omega^2(C_s + C_p + C_f)^2}} \tag{3.1}$$

Having considered white noise sources, the SNR has two trends: at low frequencies the current generators are dominant, therefore the overall noise is almost constant, while the SNR has a +20 dB/dec slope; at higher frequencies the other terms, which are proportional to the frequency, become significant, preventing the SNR from increasing any more. At one decade beyond the corner frequency the SNR can be approximated with this expression:

$$SNR_{max} = \frac{A_0 \Delta C}{\sqrt{BW}\sqrt{S_{V,s}C_s^2 + S_{V,opamp}(C_s + C_p + C_f)^2}} \tag{3.2}$$

Clearly, the circuit is going to work at sufficiently high frequencies, in order to maximize the SNR. The loop gain provides information on the closed loop bandwidth and on the system's stability:

$$G_{loop}(s) = -\frac{1 + sR_f C_f}{1 + sR_f(C_f + C_p + C_s)} A(s)$$

where $A(s)$ is the opamp's transfer function.

3.2.2 Components choice

The parameters determining the choice of the opamp have been discussed in the introduction; noise is so far the most critical one. It is important to notice that all the capacitances connected to the inverting input concur to amplify the opamp series noise; the sensor, trusting the FEM simulations, stays at few hundreds of fF, and it is not the dominant term in the sum. A physical capacitance of 1 pF has been placed as C_f, which is among the lowest available values for a discrete capacitor; the lower C_f, the better the desensitization from the following noise sources. The amplifier thus provides a voltage attenuation between 0.1 and 1. It might sound illogic to have a preamplifier with gain less than 1, but this is not an issue: the actual signal is the current from the capacitive sensor, which is transduced into an output voltage by C_f; it is sufficient to provide an output signal greater than the noise of the following stage. Moreover, this voltage attenuation allows to stimulate the sensor with a larger sinusoid, thus providing a higher current signal and SNR, without exceeding the output voltage range.

First of all, the opamp may be chosen depending on the required bandwidth, which is a quite trivial computation. The closed loop bandwidth will be approximated with the 0 dB crossing point of $|G_{loop}(j\omega)|$, which must happen with a −20 dB slope for a phase margin greater than 45°, that guarantees the system's

[2] BW is the equivalent noise bandwidth of the whole system, including the lock in demodulator; it is of the order of 1 kHz

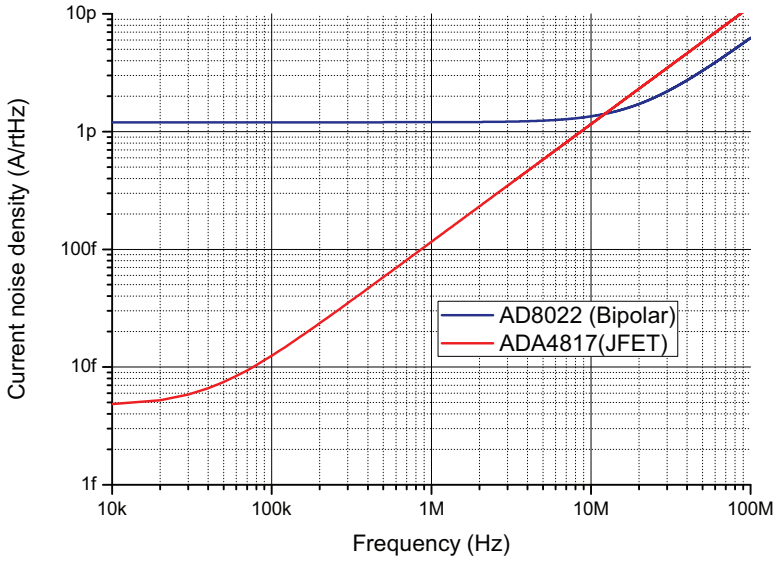

Figure 3.3: Current equivalent noise entering virtual ground, for two different opamps.

stability with a sufficiently flat step response. We are going to use a fully compensated opamp, for the crossing frequency depends on capacitance values that are not precisely predictable. The zero's time constant is 1 ms, while the pole's time constant is even lower, for it contains the same resistance, but a higher capacitance; the crossing frequency can be therefore approximated by

$$GBWP\frac{C_f}{C_f + C_p + C_s}$$

where $GBWP$ is the opamp's gain-bandwidth product in Hertz. The parasitic capacitance is of the order of some pico Farad, so the capacitive partition may be equal to $1/5$ in the worst case; the opamp is required to have a GBWP of at least 50 MHz.

Let's now discuss noise requirements. Equation 3.2 shows that in order to optimize the maximum SNR, not only the series noise generator must be as low as possible, but also the sum of all the capacitances that are connected to the non-inverting input node, which include the opamp's input capacitance (both differential and common mode ones). The overall current noise entering the virtual ground (see eq. 3.1) has been plotted in figure 3.3, for two commercial opamps: the AD8022, implemented in bipolar technology, and the ADA4817, which employs JFET transistors.

Using equation 3.1, the corner frequency can be calculated:

$$f_{nc} = \sqrt{\frac{4kT/R_f + S_{I,opamp}}{S_{V,opamp}(C_s + C_p + C_f)^2}}$$

	i_n ($fA/\sqrt{Hz}$)	e_n ($nV/\sqrt{Hz}$)	C_{in} (pF)	f_{nc} (Hz)	GBWP (MHz)
AD8022	1200	2.5	0.7	19.6 M	130
ADA4817	2.5	4	1.4	40.8 k	400
OPA657	1.3	4.8	5.2	16.8 k	1600

Table 3.1: Opamps parameters.

The noise from the signal generator has been neglected, since the opamp's series generator sees a greater overall capacitance;R_f has been chosen equal to 1 GΩ; C_s to 200 fF; C_p is the sum of the opamp's parasitics, and the PCB traces capacitance, which has been estimated in 2 pF.

Bipolar technology allows very low series noise, while keeping a relatively low input capacitance, which both concur in decreasing the optimum SNR; however, the extremely high current noise shifts the corner frequency beyond 10 MHz, where the time delays become significant, making it difficult to work in the maximum SNR interval. The suggested comparison shows a theoretical advantage of a factor of two in using the bipolar opamp, but only at high frequencies; therefore, all the efforts were directed to JFET opamps, which also have superior performances in terms of 1/f noise. MOSFET opamps can also provide both low current and voltage noise, but they have a too high input capacitance, beside suffering from 1/f noise. The two most suited opamps are the ADA4817, which has been already discussed, and, as an alternative, the OPA657 (which is not fully compensated); finally the ADA4817 was chosen.

3.2.3 PSPICE simulations

The circuit has been simulated with PSpice, using the opamp's model, in order to verify the transfer and stability performances (see fig. 3.4). The loop gain's 0 dB crossing frequency happens at about 160 MHz, a bit before than the closed loop bandwidth, which is about 200 MHz. The phase margin approaches 80°, a very conservative value. The feedback capacitive divider is also equal to the ratio of the middle frequency loop gain with respect to the low frequency one; it is a factor 4.5, different from the ratio between the closed loop bandwidth and the opamp's GBWP, so its PSpice model must have a different GBWP than stated in the datasheet. Anyway, the bandwidth and stability specifications seem to be fully reached. The voltage transfer should be, as indicated, equal to 0.2, but it depends on the actual sensor capacitance.

Noise simulations have not been performed, since the models usually disagree with the actual values. By setting to 1 the maximum SNR of equation 3.2, the nominal parameters of the ADA4817 give a minimum detectable signal of 0.58 aF with 1 V sinusoid applied at the input. Since the output dynamic range is about 3.5 V_p, corresponding to 17.5 V_p at the input node, one should be able to detect 33 zF, provided that the sensor can sustain such a voltage. These are very promising values, but only the opamp's noise has been considered: external disturbs and the signal generator noise will have to be faced in real measurement operations.

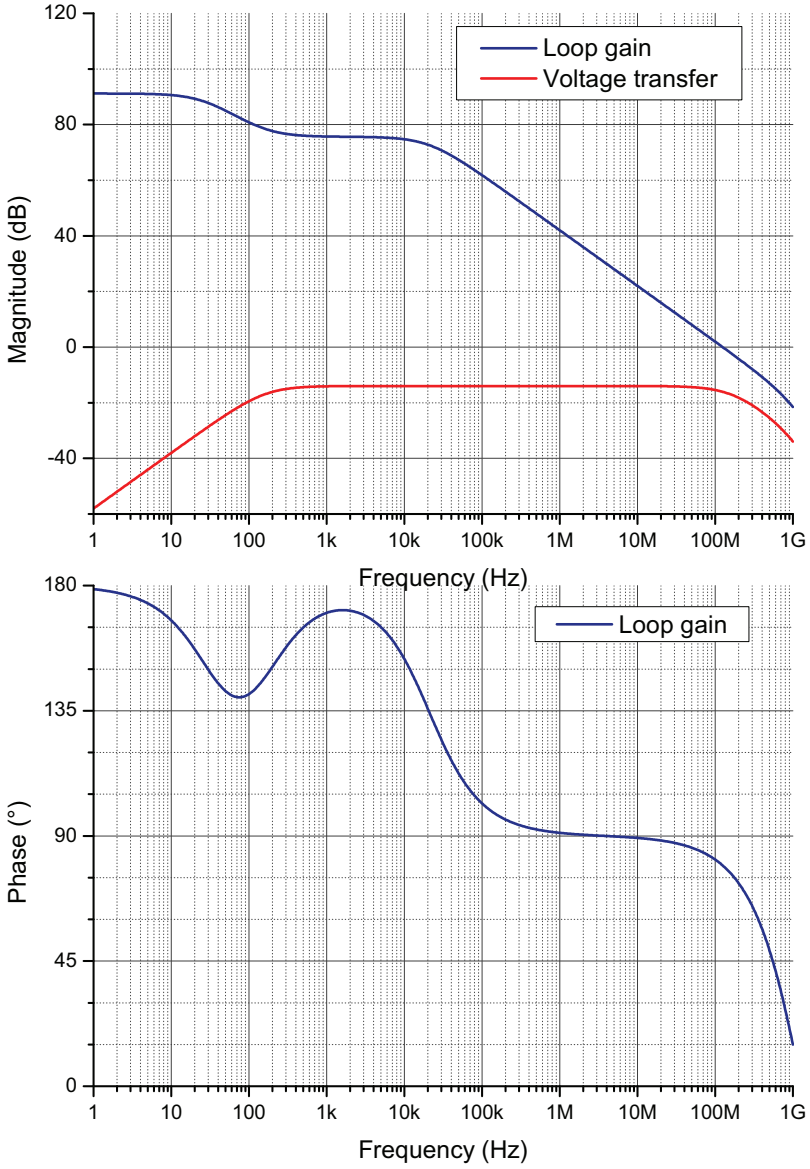

Figure 3.4: Magnitude and phase of voltage transfer and loop gain from PSpice simulations.

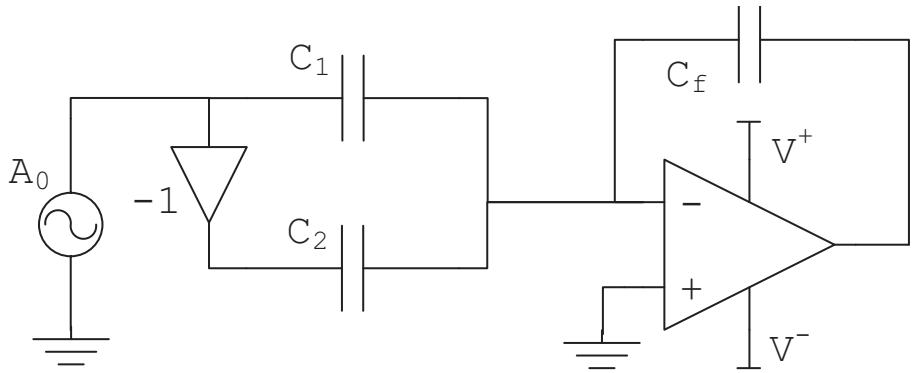

Figure 3.5: Differential measurement front-end.

3.3 Inverting buffer

Differential measurements suppress the reference high-swing reference sinusoid, which does not carry any information, while producing an output signal when the sensor's capacitance varies. With reference to fig. 3.5, and considering a single pole inverting stage, with time constant equal to τ_{inv}, one can derive the expression of the output voltage as a function of the input voltage and of the capacitance difference $\Delta C = C_2 - C_1$:

$$V_{out} = V_{in}\left(\frac{C_2}{1+s\tau_{inv}} - C_1\right)\frac{1}{C_f} = V_{in}\frac{\Delta C}{C_f}\frac{(1-sC_1/\Delta C\tau_{inv})}{(1+s\tau_{inv})} \tag{3.3}$$

For a perfectly matched couple of sensors ($C_1 = C_2$), this equation reduces to

$$V_{out} = -V_{in}\frac{C_1}{C_f}\frac{s\tau_{inv}}{1+s\tau_{inv}} \tag{3.4}$$

so only at DC the output is exactly null in that case; by increasing the operative frequency, the inverting gain gets degraded, and becomes negligible a decade beyond the buffer's cutoff frequency ($1/(2\pi\tau_{inv})$, and we return to the single sensor voltage transfer. If the two sensor are not perfectly equal, due to the presence of Particulate Matter, or, more likely to the unavoidable manufacturing mismatches, a low frequency gain equal to $\Delta C/C_f$ appears, which can be rewritten as:

$$\frac{\Delta C}{C_1}\frac{C_1}{C_f} \tag{3.5}$$

This is also the transfer function of the noise from the generator, and it corresponds to the single sensor voltage transfer, but with an attenuation equal to the relative matching of the pair of sensor: if a factor of ten attenuation is desired, the two sensors must have a ten percent matching, at least. In order to reduce the noise coming along with the input reference, either the sensor's absolute value has to be as low as possible, and the couple has to be matched. Furthermore, if this attenuation must be maintained over the entire frequency range (10 MHz), the pole of the inverting buffer has to be located at least at 100 MHz.

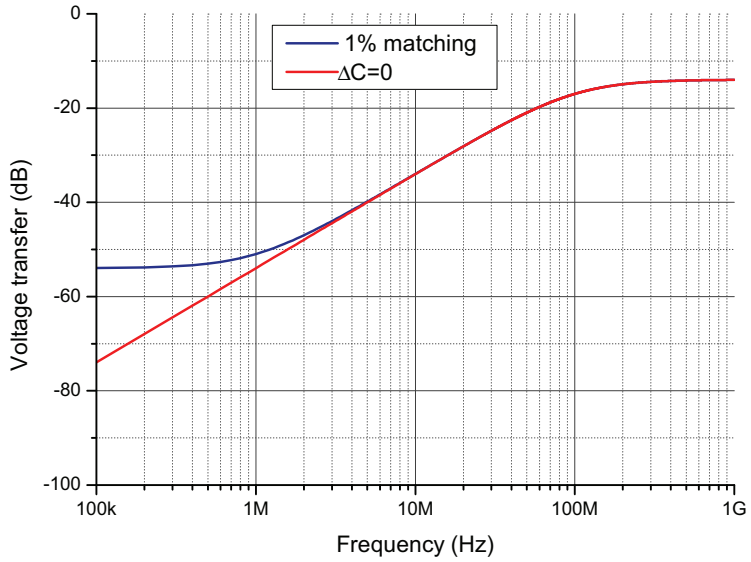

Figure 3.6: Voltage transfer function for a differential measurement, for matched and mismatched sensors.

Figure 3.6 considers two sensors, when perfectly matched, and when matched at 1%. Being the inverting stage's pole at 100 MHz, the maximum attenuation within the band of interest (10 MHz) still remains of a factor of ten; however, this is not the ultimate limit: if one backs off until 1 MHz, the attenuation becomes 40 dB with respect to the single sensor measurement, and then it finally stops dropping. The high frequency transfer is −14 dB, the sensors having an average value of about 200 fF, and the feedback capacitor being 1 pF.

Of course, this stage must not worsen the overall noise performance of the front-end. Figure 3.7 shows two possible implementations. A fully differential inverting configuration, acting as a BalUn, produces a floating voltage reference (3.7a): when everything is perfectly symmetrical, the current recirculates among the two sensors; if a capacitive variation happens, a small fraction of current leaks into virtual ground. It might seem a pleasant solution for its symmetry, but the fully differential amplifier's output common mode noise would flow entirely into the virtual ground. A simple single-ended inverting stage will be then employed (3.7b).

The noise contributions will be referred to the opamp's output voltage, and then converted into virtual ground current after the sensor's capacitance. Thermal noise from the two resistances is transferred at the output directly; being the two sources uncorrelated, a single contribution can multiplied by a factor $\sqrt{2}$. A 1 kΩ resistor carries 4 nV/$\sqrt{Hz}$, equal to the ADA4817 series noise; however, the former drops on a capacitance of few hundreds of femto Farad, whilst the latter 'drops' on some pico Farads (see eq. 3.1). If two resistances of 680 Ω are chosen, their noise contribution is not significant, so we can neglect it. The opamp's

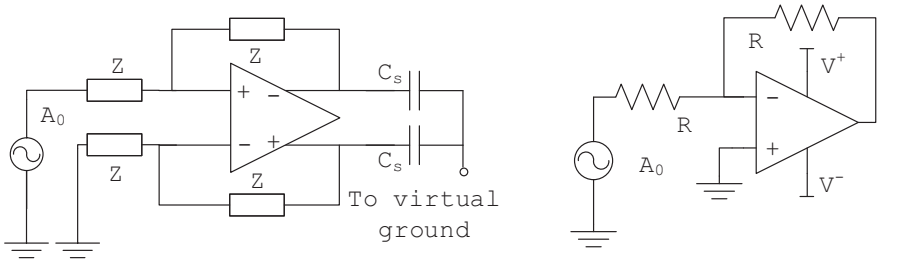

(a) *Fully differential.* (b) *Classic single-ended inverting stage.*

Figure 3.7: Two possible implementations of the inverting stage.

series and parallel noise generators, S_v and S_i respectively, are transduced into this current noise at the virtual ground of ADA4817:

$$S_v(2\omega C_s)^2 + S_i(\omega R C_s)^2$$

this current should be much lower than the ADA4817 current noise at virtual ground:[3]

$$S_{v,ADA4817}\omega^2(2C_s + C_p + C_f)^2$$

We can neglect the inverter opamp's current noise, too: common values are of the order of $1\,\text{pA}/\sqrt{Hz}$, corresponding to $0.68\,\text{nV}/\sqrt{Hz}$at the inverter output node. At last this condition must hold:

$$\sqrt{S_v} < \sqrt{S_{v,ADA4817}}\left(1 + \frac{C_p + C_f}{2C_s}\right)$$

The right-hand-side of the last inequality is about $48\,\text{nv}/\sqrt{Hz}$; an opamp with a series generator of $5\,\text{nV}/\sqrt{Hz}$ will be suited for the inverting stage, and this is just the case for the THS3001, a high speed Current Feedback Amplifier (CFA), having an equivalent input voltage noise of $1.6\,\text{nV}/\sqrt{Hz}$. Actually its negative input current noise is much more higher with respect to the previous considerations, being equal to $16\,\text{pA}/\sqrt{Hz}$; nevertheless, it corresponds to $11\,\text{nV}/\sqrt{Hz}$ at the THS3001 output, or $5.5\,\text{nV}/\sqrt{Hz}$ at its positive input, which fits the specifications.

According to the datasheet, an inverting stage with $680\,\Omega$ feedback resistors and $\pm 15V$ power supply guarantees a $-3\,\text{dB}$ closed loop bandwidth of about 400 MHz. Its $6500\,\text{V}/\mu\text{s}$ slew rate allows to work with full power on the entire bandwidth of 10 MHz, as well as the output current is sufficient to drive a 200 fF capacitive load; the ADA4817 is not limited by output slope issues, too.

3.4 PCB design

The measurement of Particulate Matter will be performed using the basic circuits designed in the previous sections, although some alternatives will be analyzed

[3]Now the ADA4817 series noise drops on a double sensor capacitance, since the differential measurements employs two equal sensors.

later. The acquisition section consists of a bottom board, that accommodates the electronics and a custom socket for the sensors slides. Every single slide was attached on a properly shaped piece of glass fiber substrate (FR-4), which has the correct pin arrangement to fit the socket. The sensors slide was bonded to these pins by means of a silver paste.

The electronics include the transimpedance and the single ended inverter, which have both been terminated with a 50 Ω resistor, in order to maintain the circuit's stability when driving a capacitive load, and to perform impedance matching with the coaxial cable that reads the circuit's output. The power supply is external; it has been chosen to ±15 V, so that the inverting stage is able to provide a high swing reference sinusoid to the sensor. Two voltage regulators must have been added, to shift the power supply level to ±5 V for the ADA4817. The MC79M05 and MC78M05 linear regulators have been chosen. The circuit receives external power supply, as well as the signal voltage reference, while providing the output of the transimpedance, through BNC connectors. Decoupling capacitors have been added, as suggested by the components datasheets. Two metal jumpers connect the desired electrodes to the voltage references. The whole circuit fits a metal box to ensure electrical isolation.

3.5 Resonant front-end

The maximum SNR that can be obtained with the circuit employed so far is degraded by all the capacitances connected to the non-inverting input of the opamp: the series noise of the active circuit produces a current noise flowing into the virtual ground; the higher the capacitive admittance, the higher this current noise (see eq. 3.2). If all these capacitances somehow resonated with a proper inductor, the opamp's series noise would be applied on an overall infinite impedance, and ideally no current noise would flow due to this contribution.

The mentioned inductor should work on the non-inverting voltage transfer, while leaving the signal transfer unchanged, therefore one of its terminals will be connected to the opamp's inverting input; this pin must follow the voltage of the non-inverting one thanks to the negative feedback, so the signal's ideal transfer will be preserved. If we connected the other terminal of the inductor directly to ground, it would behave as a short circuit at low frequency, thus deleting the feedback at the bias point. The simplest way to save the feedback at low frequency might be a bypass capacitor in series with the inductor (see fig. 3.8). This capacitor must be large enough that within the band of interest it behaves like a very low impedance, so the series is dominated by the inductor.

The ideal voltage noise transfer function to the output node can be then evaluated:

$$1 + \frac{R_f/(1+sR_fC_f)}{sL/(1+sL(C_p+C_s)} =$$

$$= \frac{1+sL/R_f+s^2L(C_f+C_p+C_s)}{sL/R_f(1+sR_fC_f)}$$

The equivalent transadmittance to the virtual ground is obtained:

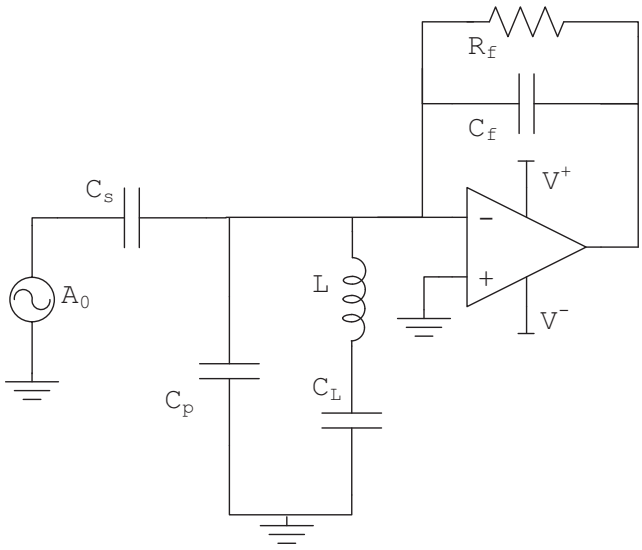

Figure 3.8: Transimpedance with inductor.

$$\frac{1 + sL/R_f + s^2L(C_f + C_p + C_s)}{sL}$$

When the inductor resonates with the sum of all the capacitances connected to the inverting input (some pico Farad), the current noise spectral density is minimized. The feedback resistance limits the quality factor of the resonance, being the ultimate impedance on which the voltage replicated at the inverted node drops; if R_f were infinite, no current noise would flow into virtual ground due to the opamp's series noise. Anyway, in this case the residual current noise would be white, and of the order of atto Ampere per root-Hertz, so the other white current noise sources would be the main contributions. There would be some improvements, indeed, for the 20 dB/dec rising part of the virtual ground current noise would be eliminated (fig. 3.3), and the SNR would rise by increasing the frequency along the entire bandwidth of interest.

Actually, that is not so immediate. One must also consider that a real inductor has a limited quality factor, and it works properly only below its antiresonance frequency. The latter drawback is equivalent to say that the inductor has a parasitic capacitance, that dominates its impedance above the antiresonance. These parasitics must not, of course, be larger than the capacitances that are intended to be made resonate. The limited inductor's quality factor can be associated to an equivalent parallel resistance R_L[4]; following the same previous procedure, the virtual ground transadmittance becomes:

[4]If the inductor's losses are represented by a parallel resistance, its quality factor can be expressed as $R_L/(\omega L)$.

$$\frac{1+sL\left(\frac{1}{R_f}+\frac{1}{R_L}\right)+s^2L(C_f+C_p+C_s)}{sL}$$

This is a quite satisfactory (and predictable) result: the passive elements compose themselves in parallel, and so does the overall quality factor, so that the lower one limits the resonance goodness.

The stability of this circuit is a rather tedious task: let's first calculate the circuit's loop gain. The inductor's series capacitance must now be included, to take into account all the singularities. Its quality factor will be considered infinite, instead. The opamp's transfer function is A(s).

$$Z_f = \frac{R_f}{1+sR_fC_f}$$

$$Z_p = \frac{1+s^2LC_L}{sC_L} || \frac{1}{s(C_p+C_s)} = \frac{1+s^2LC_L}{s(C_p+C_s+C_L)+s^3LC_L(C_p+C_s)}$$

$$G_{loop} = \frac{-A(s)Z_p}{Z_p+Z_f} = \frac{-A(s)(1+sC_fR_f)(1+s^2LC_L)}{1+sR_f(C_f+C_p+C_s+C_L)+s^2LC_L+s^3LC_LR_f(C_p+C_s+C_f)}$$

If we consider that C_s and C_p are in parallel in the loop gain calculation, four reactive elements are present, but a third order transfer has been obtained. In fact, two capacitors are linearly dependent. At low frequency the inductor is in series with a capacitor, which high impedance; all the capacitors see R_f, so the coefficient of the first degree term is the one expected; the low frequency time constant is almost equal to R_fC_L, since C_L dominates the other capacitances. At higher frequencies, we can neglect the 1 at the denominator, and gather sR_fC_L, obtaining the expression of two complex poles resonance frequency at $\omega_0 = 1/\sqrt{L(C_p+C_s+C_f)}$, and quality factor $R_f/(\omega_0 L)$. The loop gain has also three zeros: one is due to the feedback parallel RC, while the two remaining are a purely imaginary pair that nullify the loop gain at the LC series resonant frequency (the circuit closed loop gain is far different from the ideal one around this frequency, since the feedback is null).

The circuit has been simulated with PSpice, and the corresponding frequency responses are shown in fig. 3.9. The ADA4817 has been used again, with all the same parameters as in the integrator section; the inductor has been chosen equal to 100 H̆, in order to be able to resonate with some pico Farad at a reasonable frequency, between 1 and 10 MHz; a series capacitor of 2.5 nF resonates with the inductor at 320 kHz, which seems far enough from the operating frequency. With this choice, the loop gain is high enough at low frequencies in order to set the bias condition within a reasonable time interval.

The results show that the loop gain stays over 20 dB up to 10 kHz, so the bias is preserved. Around that frequency, the opamp's first pole makes it decrease, until, just at 300 kHz, the LC series becomes a short circuit, forcing it to zero. The inverting gain, which is related to the signal's transfer, stays at its ideal value of −14 dB within the band of interest, except around the LC series resonance, where it also drops to zero. The loop gain has finally an antiresonance at 7.5 MHz: the inductor is resonating with the smaller capacitances. At the same frequency, the transadmittance from the non-inverting input to virtual

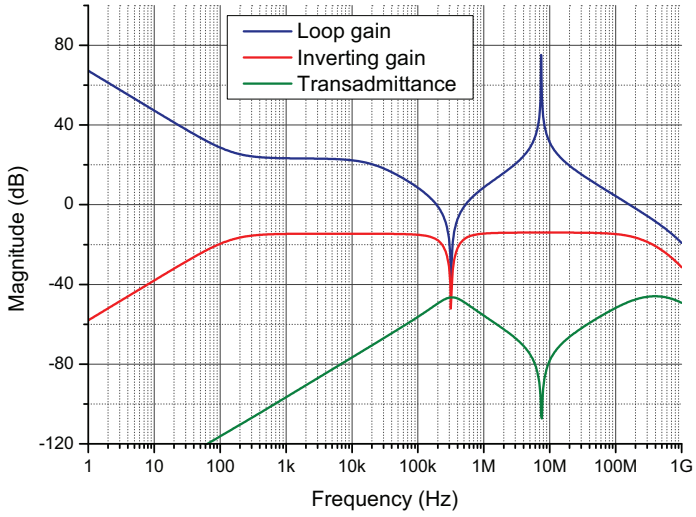

Figure 3.9: PSpice simulations of the resonant circuit proposed; the magnitude of loop gain, closed loop gain, and noise transfer to virtual ground are compared.

ground displays a notch behavior. These graphs have been taken sampling at 100 points per decade. If the rate is increased to 10 000 in the decade of interest, the simulator gives a minimum of 4.9 nS, which is closer to the expected value with respect to what shown on figure 3.9.

The stability of this circuit must be ensured. Unfortunately, the loop gain displays multiple crossings of the 0 dB ax, therefore Bode's stability criterion cannot be used. Nyquist's criterion has to be applied. Figure 3.10 is a plot of the Nyquist diagram of $G_{loop}(j\omega)$ traced with MATLAB. The control theory's approach will be followed, so, for negative feedback, a positive low frequency loop gain will be considered, while the minus sign is included into the differentiator node of the feedback block diagram. Since there are no poles with positive real part, the number of loops made by the Nyquist diagram around the point (-1,0) must be zero to have stability [16].

The Nyquist diagram never seems to enter the negative real part semi-plane, therefore it should not encircle the (-1,0) point, and the system should be stable (fig. 3.10a). However, scale is very large, so the diagram will be better analyzed with more detailed pictures to ensure the circuit is truly stable. The diagram starts at point (36 000 ,0), the loop gain at DC (fig. 3.10b). The low frequency pole curves it such that the magnitude diminishes, approaching the origin with a $-90°$ phase (fig. 3.10c). The feedback impedance's zero stops the middle frequency magnitude at 14, while bringing the phase back to zero (fig. 3.10c). The opamp's first pole creates a secondary circular bending, which would bring the magnitude towards zero with $-90°$, again; the diagram actually crosses the origin, due to the imaginary zeros pair, which also boost the phase to 90° (fig. 3.10d). This phase shift is nullified by the following complex poles pair, with a large magnitude increase that produces the outer ring (fig. 3.10e and 3.10f).

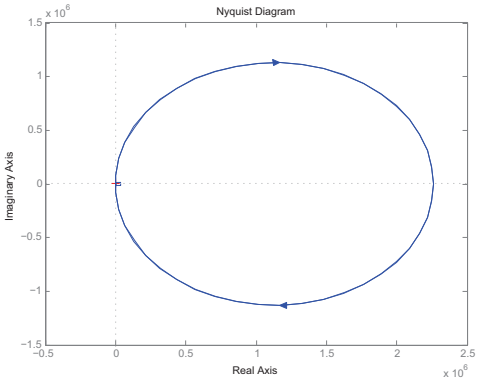

(a) *The whole Nyquist diagram lays entirely in the positive real part semi-plane.*

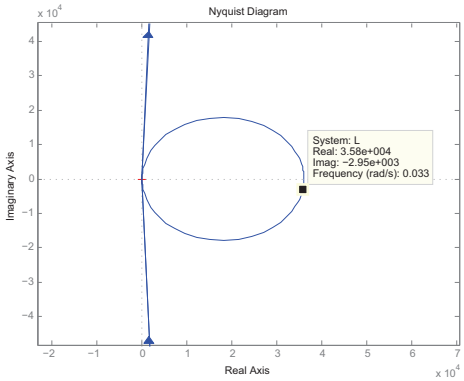

(b) *It starts at (36000,0).*

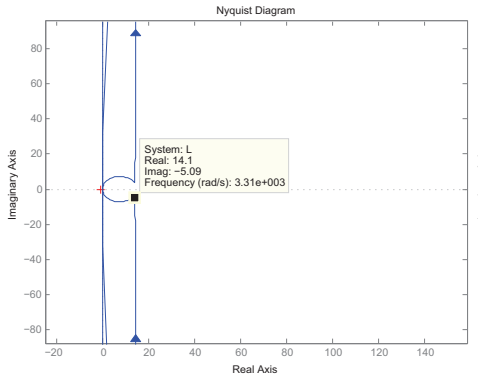

(c) *The zero fixes the middle frequency gain.*

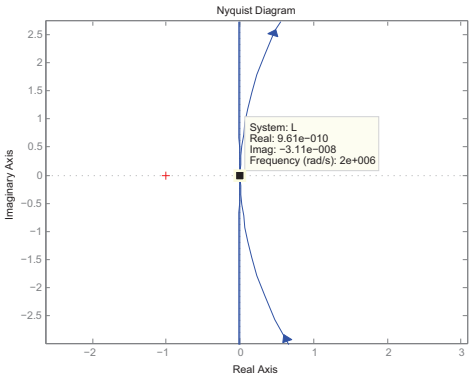

(d) *The loop gain crosses the origin when the LC series resonates.*

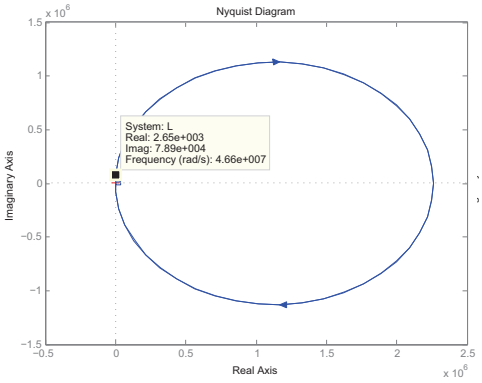

(e) *The magnitude increases with 90° phase.*

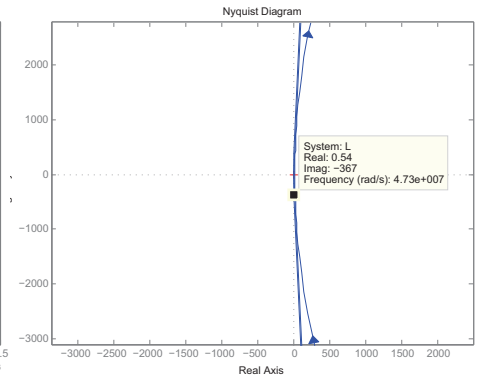

(f) *The complex poles pair produces the outer ring.*

Figure 3.10: Nyquist diagram of the resonant circuit's loop gain.

	e_n ($nV/\sqrt{Hz}$)	C_{gs} (fF)	C_f (fF)	I_{DSS} (mA)	V_p (V)
MX-20B	1.6	0.6	50	9	-2
MO-16	1.5	1.2	30	14	-3

Table 3.2: Parameters of two low-noise JFET, for I_D=5 mA, V_{sub}=−7.5 V, V_{gs}=−0.2 V.

The diagram ends with a −90° phase, approaching the origin as a single pole transfer, an absolutely stable situation.

One could now object that the opamp has more singularities, that change the diagram. This is true, but the second pole is located at 400 MHz, where the magnitude is well inferior than 1, so its effect is definitely negligible. This circuit has proven its stability, and it seems to be able to significantly reduce the front-end noise, while substantially keeping the same signal transfer, at least theoretically. Only an effective implementation may confirm all these expectations.

3.6 External JFET front-end

In section 3.2 the transimpedance had a JFET input opamp, to exploit the benefits of that technology on noise and input capacitance. The same (or a better) result may be reached by a two stage amplifier, consisting of an external, single transistor, ultra low noise JFET preamplifier, followed by an ordinary opamp. The preamplifier would determine the noise performances, since the opamp's sources would be reduced by the first stage's gain (a factor of ten); on the other hand, the opamp is needed to increase the overall open loop gain, in order to make the feedback stronger.

Table 3.2 lists the parameters of two JFETs by MOXTEK, Inc. Both voltage noise and input capacitance are better than the ADA4817. They also provide a very low feedback capacitance pin, that would desensitize the following stage's noise even better. And that is actually the whole feedback capacitance, because no parallel resistor must be inserted to fix the bias condition, for a reset pin is also available. This reset pin acts as a diode, and it activates when a negative voltage is applied, sinking current out from the gate terminal (see fig. 3.11). The circuit exhibits a negative feedback, so the drain voltage follows the opamp's inverting pin, thus fixing the drain current. The n-JFET has a reverse-bias gate current flowing out of the terminal; if we left only the capacitive network, this would cause the output of the opamp to linearly decrease, until it would reach the negative supply. With a negative reset diode, the gate bias current can flow into it, keeping the output within the dynamic range. At the same time, the diode must not absorb the signal current, so the output is low-pass filtered before being fed back to the reset pin. This bias current is less than 1 pA, corresponding to a shot noise of 0.56 fA; the reset diode small signal resistance is V_T/I_D, equal to 25 GΩ.

The capacitances at virtual ground that concur in the voltage noise transfer are now C_s (200 fF), C_{gs} (600 fF), and C_f (50 fF); due to the negative feedback, the drain node remains practically constant, so the gate-drain capacitance does

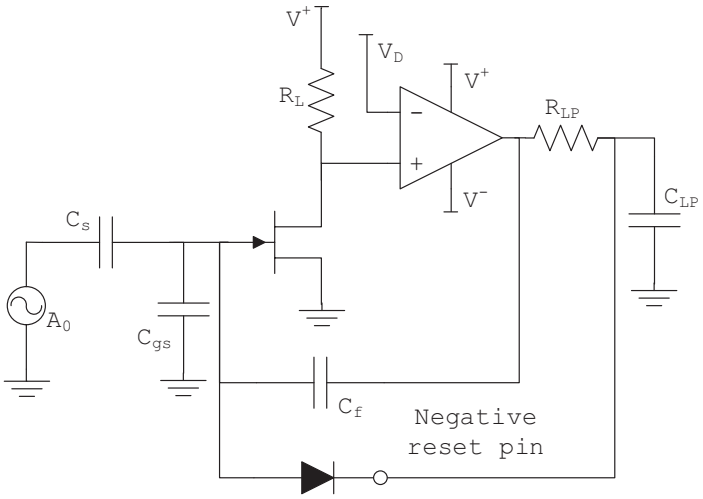

Figure 3.11: Transimpedance with low noise JFET.

not experience the Miller effect, and its value is negligible with respect to the gate-source one if the transistor operates in the saturation region. The 2 pF trace's capacitance can be avoided if a bare die device is used, bonding the gate pin directly to the sensor, so the overall contribution is 0.85 pF. Having also reduced the voltage noise of a factor of 3, the overall improvement in the SNR could be more than 10.

The bias condition can be fixed as follows: the first stage gain is the ratio between the resistor's static voltage, and the half overdrive of the JFET. For a 5 mA drain current, with the substrate at −7.5 V, the gate-source voltage should be −0.2 V; the pinch-off voltage is about −2 V. We obtain a 1.5 V overdrive, so the drain voltage can be fixed at 5 V for a gain of 13, with a 15 V positive supply. The load resistance should be 2 kΩ, and the transistor is working in saturation. The transistor's transconductance can be calculated:

$$g_m = \frac{2I_{DSS}}{V_p}\sqrt{\frac{I_D}{I_{DSS}}} = 6.7\,\text{mS}$$

The equivalent voltage noise can also be calculated:

$$e_n = \frac{4kT\gamma}{g_m} = 1.3\,\text{nV}/\sqrt{\text{Hz}}$$

which is consistent with table 3.2.

The low pass components can be chosen equal to 1 GΩ and 1 nF for a time constant of 1 s: an output voltage of 10 V at 1 MHz becomes 10 μV, therefore the diode does not interfere. Actually, this is an open loop approach. We can compute the external loop gain, considering that the two active stages along

e_n ($nV/\sqrt{Hz}$)	i_n ($pA/\sqrt{Hz}$)	GBWP (MHz)	Supply (V)	Slew rate ($V/\mu s$)	C_{in} (pF)	$G_{openloop}$ (dB)
4.5	1.5	30	±12	53	1.4	96

Table 3.3: AD8397 opamp parameters.

with C_f form an integrator, and the diode acts as 25 GΩ resistance R_D:

$$|G_{loop,ext}| \simeq \frac{1}{\omega R_D C_f} \frac{1}{\omega R_{LP} C_{LP}}$$

which is far less than 1 within the operating bandwidth. The noise of R_{LP} is not transferred to the output, either. The resistance R_L has a voltage noise of $5.6\,nV/\sqrt{Hz}$, which is divided by 13 when taken back as an equivalent series noise. The same holds for the opamp series noise, which has the same order of magnitude. Now even a bipolar opamp can be used: its current noise, which is of some $pA/\sqrt{Hz}$, gets multiplied by 2 kΩ, and then divided by 13, too.

All these noise contribution, if compared to the JFET series noise, are negligible, especially when quadratically summed. They are not concerning even when transduced into the equivalent input current generator: let's consider the noise of R_L[5]:

$$e_{n,out} = \sqrt{4kTR_L}|A(j\omega)|$$

$$e_{n,out} = \frac{i_{n,eq}}{\omega C_{gs}} 10|A(j\omega)|$$

$$i_{n,eq} = \frac{\sqrt{4kTR_L}}{10}\omega C_{gs}$$

It is about ten times lower than the current noise produced by the JFET series generator.

A suited opamp could be the AD8397, which is unitary gain stable (see table 3.3). Although it does not reach the exact slew rate for full power bandwidth, it can work with a 1 V input reference up to 2.1 MHz; its CMRR is equal to −96 dB, so the 5 V input common mode voltage is replicated at the output at DC, and an output voltage of 4 V can be sustained. Both these restriction can be easily overcome by performing differential measurements, which would determine an output swing of some hundreds of mV.

Now the loop gain expression can be obtained, after some calculations. Let's apply a test voltage V_T at the output node, after the loop has been cut. The KCL at the gate node can be written as:

$$(V_g - V_T)sC_f + V_g sC_1 + (V_g - V_d)sC_{gd} = 0 \tag{3.6}$$

where $C_1 = C_s + C_{gs}$. The KCL at the drain node holds (C_2 is the opamp's input capacitance):

$$V_g g_m + V_d(1/R_L + sC_2) + (V_d - V_g)sC_{gd} = 0 \tag{3.7}$$

[5]For the calculation of the parallel generator, the circuit's input must be left open circuit.

By merging these two equations, the drain voltage is obtained as a function of the test voltage; finally the loop gain expression can be highlighted, by multiplying the drain voltage for the opamp's transfer function $A(s)$:

$$G_{loop}(s) = -\frac{C_f}{C_f + C_1 + C_{gd}(1 + g_m R_L)} \frac{g_m R_L (1 - sC_{gd}/g_m)}{1 + sR_L \frac{(C_1+C_f)(C_2+C_{gd})+C_{gd}C_2}{C_1+C_f+C_{gd}(1+g_m R_L)}} A(s)$$

The bias network has been neglected, being its singularities at very low frequencies. The DC gain, apart from the opamp's transfer, is a capacitive divider (which also includes the equivalent Miller capacitance at the gate node), multiplied by the gain of the common source stage. The well known right-semi-plane zero of the common source would be located at 18 GHz, if C_{gd} were 1/10 of C_{gs}. The low frequency loop gain equals 93 dB, producing a gain bandwidth product, with the 300 Hz pole, of 13.4 MHz. The only pole due to the four capacitors (there are two linearly independent meshes, and a pole-zero cancellation in the origin), whose complete expression has been highlighted, is located at 91 MHz. The 0 dB crossing's slope would be −20 dB, ensuring the system's stability.

Chapter 4

Circuit characterization

The lock-in measurement will be performed by a commercial device by Zurich Instruments, the HF2LI digital lock-in amplifier. While providing the sinusoidal reference from a DAC, it converts the output of the transimpedance by means of an ADC; the digitized signal is then demodulated. The transfer and noise features of the analog stage alone will be first discussed, and then the whole system will be studied.

4.1 Transfer functions

Measurements of the circuits gain and bandwidth have been obtained by the Agilent E5061B Network Analyzer. Figure 4.1 shows magnitude and phase frequency response of the transimpedance and inverting buffer cascade, when a discrete 10 pF capacitor is connected at virtual ground. The middle frequency gain is 17 dB, from which a 1.4 pF value for the feedback capacitor can be guessed. Before 150 Hz, the transfer is rising by 20 dB/dec, owing to the feedback resistance. The closed loop bandwidth is around 20 MHz, which is lower than the simulated value, for the large test capacitance diminishes the loop gain's crossing frequency; it fully complies the design specification anyway. The middle frequency phase stands at 0°, because the signal undergoes two sign inversions. A differential measurement with two 10 pF capacitors proves that they are matched within 1%; the red curve follows the differential transfer anticipated in the design section, with a zero-pole pair, although the pole is due to the transimpedance's limited bandwidth, and not to the buffer's. The buffer's frequency response has been measured separately (figure 4.2). It has a -0.6 dB gain, and a 200 MHz bandwidth.

Now that the feedback capacitance is known with accuracy, we can repeat the same kind of measurement with the coplanar sensors, in order to extract their total capacitance, and the system's maximum bandwidth. Let's consider the slide B of wafer 2; the sensor's name is made according to the layout section, so electrodes 2B-2d refers to the sensor of wafer 2, slide B, the second of group d, and so on. Each sensor has been connected to the network analyzer's voltage source, and tested by the transimpedance. The overall voltage transfer is shown in figure 4.3; at middle frequency the magnitude is C_s/C_f, where $C_f = 1.4\,\text{pF}$. The group 'd' electrodes of slide B have constant gap and length

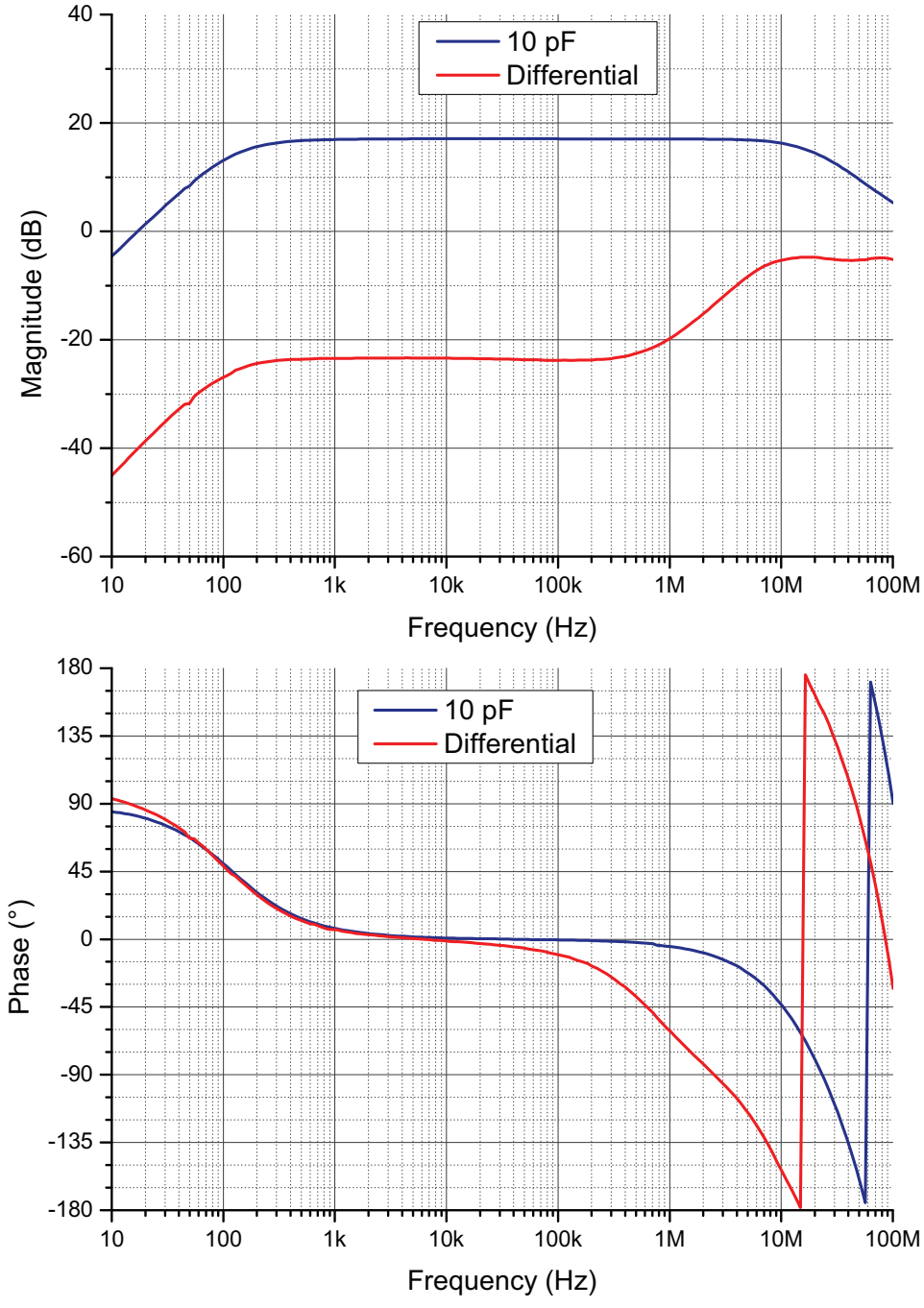

Figure 4.1: Transimpedance and inverting buffer cascade measured transfer function.

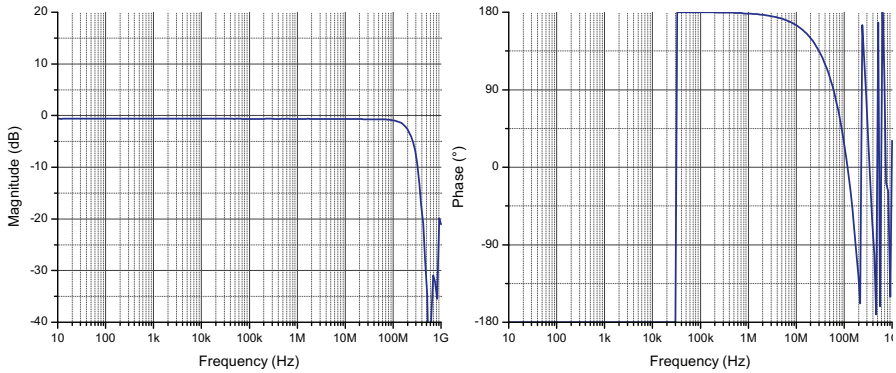

Figure 4.2: Inverting buffer measured frequency response.

increasing with code number, so the capacitance should also increase. The data prove this trend, but this is probably due to the stray capacitances of the traces: electrodes of group "s" have all been designed equal, but they also differ in their absolute capacitance. The capacitance measured values at 1 MHz are listed in table 4.1f: though remaining of the order of a few femto Farad, they are higher than expected after the simulations, therefore the parasitics must be all but negligible. Anyway, the order of magnitude is compliant to the expectations, as well as the transfer's shape, which depicts a frequency independent capacitance for almost every pair, and suggests a -3 dB bandwidth around 70 MHz.

Sensors 2B-1d and 2B-2d, although designed differently, show a very high matching, so they have been connected to have a common terminal, to be able to perform differential measurements; the resulting transfer is also shown on figure 4.3. It does not faithfully reproduce the expected differential transfer, but it displays a minimum plateau region just in the bandwidth of interest, at -26 dB below the single transfer, meaning a 4% matching. The lower frequencies ripples must not concern: they are orders of magnitude less than the sensor's absolute value. This connection was done whenever two sensor looked sufficiently matched. The resulting residual capacitance differs from the exact difference between them: the soldering operation perturbs the initial capacitance values.

Table 4.1 and table 4.2 list the capacitances, which are generally close for respective slides of different wafers. The missing values refer to damaged or short-circuited sensors. This last issue involves every pair with gap equal to 2 μm, which was the manufacturing resolution.

The gap qualitative dependence has been verified: slides C and D have a decreasing capacitance with a decreasing gap, though the traces length is increasing; in slides A this is partially true, because for the furthest pairs, which have the longest traces, the capacitance returns to increase.

4.2 Noise

The noise characterization was carried both in time and frequency domain: the rms value has been evaluated with a lock-in filtering around the frequency of interest (1 MHz for most of the cases); at the same time the Agilent N9020A

Sensor	|Gain|	C_s (fF)
1A-1s	0.384	538
1A-2s	0.346	485
1A-3s	0.339	474
1A-2s3s	0.013	18
1A-1d	/	/
1A-2d'	0.538	753
1A-2d"	0.507	710
1A-3d	0.146	205
1A-4d'	0.131	184
1A-4d"	/	/
1A-5d	/	/

(a) *Slide 1A.*

Sensor	|Gain|	C_s (fF)
1B-1s	/	/
1B-2s	/	/
1B-3s	/	/
1B-1d	/	/
1B-2d	0.143	215
1B-3d	0.160	239
1B-4d	/	/
1B-5d	0.223	223
1B-2d3d	0.008	11

(b) *Slide 1B.*

Sensor	|Gain|	C_s (fF)
1C-1s	/	/
1C-2s	0.349	488
1C-3s	0.301	421
1C-1d	/	/
1C-2d	0.165	231
1C-3d	0.118	165
1C-4d	0.107	151
1C-5d	0.108	151

(c) *Slide 1C.*

Sensor	|Gain|	C_s (fF)
1D-1s	0.318	445
1D-2s	0.290	407
1D-3s	0.291	408
1D-2s3s	0.011	15
1D-1d	/	/
1D-2d	0.192	269
1D-3d	0.146	205
1D-4d	0.137	193
1D-5d	0.136	191
1D-4d5d	0.023	33

(d) *Slide 1D.*

Sensor	|Gain|	C_s (fF)
2A-1s	/	/
2A-2s	0.302	424
2A-3s	0.284	398
2A-1d	/	/
2A-2d'	/	/
2A-2d"	/	/
2A-3d	0.136	190
2A-4d'	0.115	162
2A-4d"	0.126	177
2A-5d	0.139	194
2A-2d-diff	/	/
2A-4d-diff	0.014	19

(e) *Slide 2A.*

Sensor	|Gain|	C_s (fF)
2B-1s	0.329	461
2B-2s	0.288	404
2B-3s	0.249	349
2B-1d	0.115	160
2B-2d	0.116	162
2B-3d	0.123	173
2B-4d	0.147	205
2B-5d	0.180	251
2B-1d2d	0.006	8.4

(f) *Slide 2B.*

Table 4.1: Sensor capacitance derived from voltage transfer.

Sensor	|Gain|	C_s (fF)
2C-1s	0.336	470
2C-2s	0.345	483
2C-3s	0.294	412
2C-1d	/	/
2C-2d	0.159	222
2C-3d	0.111	155
2C-4d	0.098	137
2C-5d	0.097	135

(a) *Slide 2C.*

Sensor	|Gain|	C_s (fF)
2D-1s	0.342	478
2D-2s	0.303	425
2D-3s	0.297	416
2D-2s3s	0.012	17
2D-1d	/	/
2D-2d	/	/
2D-3d	0.147	206
2D-4d	0.135	189
2D-5d	0.133	186
2D-4d5d	0.024	34

(b) *Slide 2D.*

Sensor	|Gain|	C_s (fF)
4A-1s	0.331	497
4A-2s	0.292	438
4A-3s	0.253	379
4A-1d	0.188	282
4A-2d'	0.133	199
4A-2d"	0.128	192
4A-3d	0.115	161
4A-4d'	0.116	162
4A-4d"	0.129	181
4A-5d	0.152	227
4A-2d-diff	0.006	9.45
4A-4d-diff	0.013	19.0

(c) *Slide 4A.*

Sensor	|Gain|	C_s (fF)
4B-1s	0.346	519
4B-2s	0.308	462
4B-3s	0.255	383
4B-1d	0.128	192
4B-2d	0.129	194
4B-3d	0.159	239
4B-4d	/	/
4B-5d	0.222	333
4B-1d2d	0.001	1.5

(d) *Slide 4B.*

Sensor	|Gain|	C_s (fF)
4C-1s	0.348	522
4C-2s	0.304	457
4C-3s	0.299	448
4C-2s3s	0.017	24
4C-1d	/	/
4C-2d	0.164	246
4C-3d	0.115	172
4C-4d	0.103	155
4C-5d	0.106	158
4C-4d5d	0.008	11

(e) *Slide 4C.*

Sensor	|Gain|	C_s (fF)
4D-1s	0.314	439
4D-2s	0.285	399
4D-3s	0.285	399
4D-2s3s	0.013	19
4D-1d	/	/
4D-2d	0.188	264
4D-3d	0.141	197
4D-4d	0.129	181
4D-5d	0.127	177
4D-4d5d	0.025	34

(f) *Slide 4D.*

Table 4.2: Sensor capacitance derived from voltage transfer.

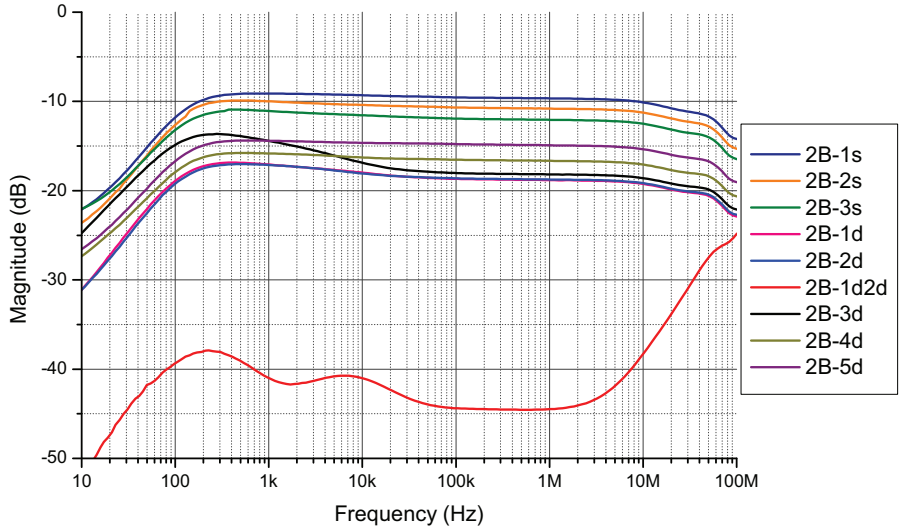

Figure 4.3: Frequency response of the front-end connected to the slide 2B sensors.

IN range (V_p)	0.001	0.01	0.1	1
e_n ($nV/\sqrt{Hz}$)	5	5	9	60

Table 4.3: HF2LI lock-in AC coupling input voltage noise.

MXA Spectrum Analyzer has been employed to measure the noise spectral density. The expected rms voltage noise at transimpedance output , with no sensor connected, should be:

$$v_{rms,out} = e_{n,ADA4817}\left(1+\frac{C_p}{C_f}\right)\sqrt{BW} = 4\,\text{nV}/\sqrt{\text{Hz}}\left(1+\frac{2\,\text{pF}+1.4\,\text{pF}}{1.4\,\text{pF}}\right)\sqrt{1\,\text{kHz}}$$

the first factor corresponding to the output voltage spectral density ($13.7\,nV/\sqrt{Hz}$), producing a $0.43\,\mu V$ noise on the signal's bandwidth. The HF2LI lock-in also carries its own input-referred noise, which varies according to the selected input voltage range (see table 4.3). As long as this instrument will be employed, the voltage range is quite limited: in order to keep its noise negligible, the maximum reference voltage amplitude should be 300 mV with a single sensor measurement. The amplitude can be increased if differential measurement are performed; in this case a lower input range can be selected, keeping the lock-in input noise at its minimum.

At first, a characterization of the lock-in itself has been done: a time domain voltage waveform after lock-in filtering was recorded, keeping the HF2LI input short-circuited, and then the rms value was calculated (see fig. 4.4). The measurements confirm the data on the user's manual (table 4.4). Then, the transimpedance was connected to the HF2LI, but still with no sinusoid applied (table 4.5), and with its virtual ground open-circuited. The datum at 1 MHz is very close to the expectations; at higher frequency the lock-in input capacitance

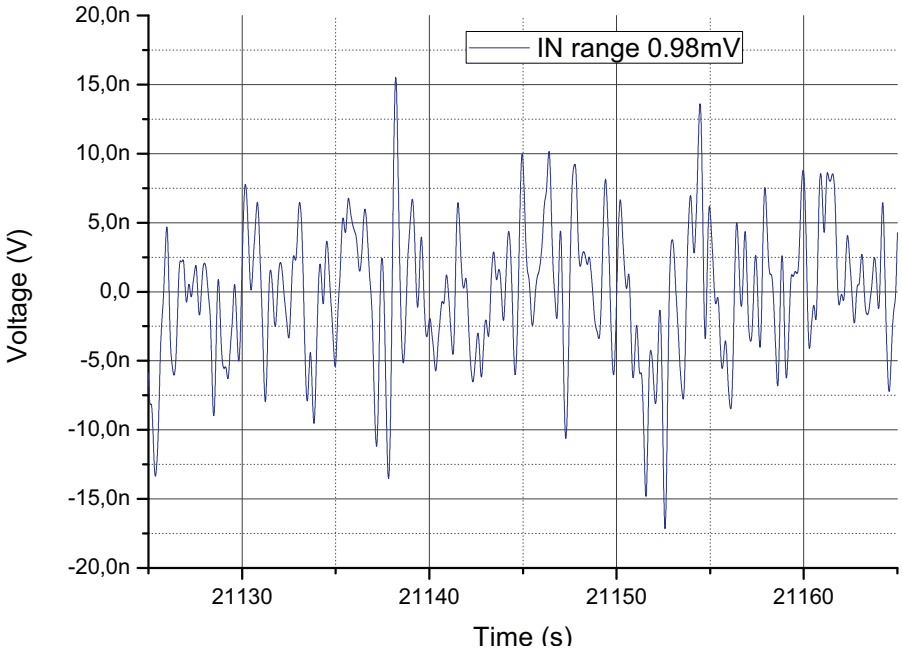

Figure 4.4: Voltage waveform after lock-in filtering, with reference frequency of 1 MHz, noise equivalent bandwidth of 1.1 Hz, and short circuited input port (IN range of 0.98 mV).

Frequency (MHz)	Bandwidth (Hz)	IN range (V)	Voltage rms (nV)	e_n ($nV/\sqrt{Hz}$)
1	1.1	0.98 m	4.80	4.36
1	1.1	81 m	8.60	7.82
1	1.1	130 m	12.3	11.2
1	1.1	0.98	45.5	41.4
1	1.1	2	76.3	69.4

Table 4.4: HF2LI lock-in input voltage noise, measured for different input ranges.

Frequency (MHz)	Bandwidth (Hz)	IN range (V)	Voltage rms (nV)	e_n (nV/$\sqrt{\text{Hz}}$)
10	1.1	0.98 m	15.4	14.0
1	1.1	0.98 m	19.1	17.4
0.1	1.1	0.98 m	46.5	42.3
0.01	1.1	0.98 m	153	139
1	1.1	81 m	20.7	18.8
1	1.1	130 m	27.7	25.2
1	1.1	0.98	53.3	48.4
1	1.1	2	86.8	78.9

Table 4.5: Transimpedance output voltage noise.

Frequency (MHz)	Bandwidth (Hz)	IN range (V)	Voltage rms (nV)	Circuit
1	1.1	0.98 m	24.4	B, 1A-2s, T
1	1.1	0.98 m	21.7	B, 1A-1s, T
1	1.1	0.98 m	25.0	1A3s, T
1	1.1	0.98 m	22.7	1A1s, T

Table 4.6: Transimpedance, buffer, and sensors output voltage noise (B=buffer, T=transimpedance).

acts as a filter, so the 10 MHz value is not useful. At lower frequencies the noise should increase, due to the 1/f contributions, and the white current noise of the opamp. If higher input ranges are chosen, the noise also increases, accordingly. If the inverting buffer is added, along with a sensor, the overall noise does not show a significant worsening (table 4.6). The spectral analysis confirms the time measurements (fig. 4.5). The low frequency noise is $4\,\mu\text{V}/\sqrt{\text{Hz}}$, i.e. the thermal noise of a 1 GΩ resistor. At about 100 Hz the feedback capacitance becomes more conductive, therefore the white current noise gets integrated; the drop is not infinite: at high frequency the opamp's voltage noise is transferred to the output, according to the non-inverting gain. The measured curve is slightly different from the theoretical one, since the slope is a bit less than −20 dB/dec, and also the high frequency plateau is about $20\,\text{nV}/\sqrt{\text{Hz}}$, which is higher than expected, although very close. Actually, below 100 kHz, the opamp produces a significant amount of 1/f voltage noise, with a 3 dB corner frequency at 10 kHz. According to the opamp's datasheet, the 1/f slope is −10 dB/dec up to 100 Hz, beyond which it becomes steeper. The 1/f noise has been included in the theoretical spectrum, and R_f was also considered in the feedback impedance, giving this formula:

$$e_{n,out}^2 = \frac{R_f^2}{1+(\omega R_f C_f)^2}\left\{S_i + \frac{4kT}{R_f} + \frac{1+[\omega R_f(C_f+C_s+C_p)]^2}{R_f} S_v\left(1+\frac{\omega_{nc}}{\omega}\right)\right\}$$

where S_v and S_i are the opamp white noise power spectral densities. By looking at figure 4.5, 1/f noise contribution is not visible even in the theoretical spectrum, so it is unlikely to be the cause of the different shape around 100 kHz.

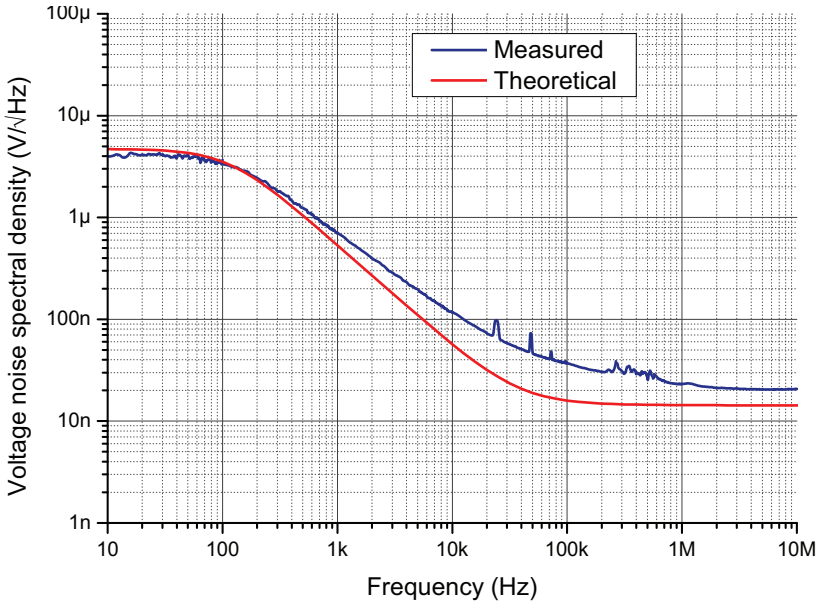

Figure 4.5: Measured voltage noise spectral density at the output node of the transimpedance.

Anyway, the overall trend is compliant with the theory, and beyond 1 MHz the spectral density is comparable to the expected value, proving to be the most suitable working frequency interval.

At this point the overall measurement setup, including the sinusoidal reference provided by the HF2LI, must be tested: this final analysis led to a very disappointing result. The noise contribution from the signal generator, which had always been neglected in the previous sections, turned out to be the main contribution (see table 4.7).

According to the lock-in user's manual, the output DAC that provides the sinusoidal reference should carry a $25\,\mathrm{nV}/\sqrt{\mathrm{Hz}}$ white voltage noise, which drops on a 500 fF sensor capacitance in the worst case, according to the previous measurements; the sum of all the capacitances at virtual ground, which determine the opamp's contribution to the overall noise, are ten times higher; the equivalent DAC noise at the opamp's non-inverting pin is $2.5\,\mathrm{nV}/\sqrt{\mathrm{Hz}}$, therefore it should be negligible. The first row of table 4.7, instead, shows a value more than two orders of magnitude higher when the sensor is stimulated by the lock-in voltage reference. The second row shows a differential measurement with the same other parameters: the noise drops significantly (about 20 times), although the spectral density is still too much intense; this proves it must come along with the voltage reference. The third row deals, again, with a single sensor measurement, having reduced the reference by 1/12; the resulting noise dropped by 1/6, so this noise is amplitude dependent. We can see it also in rows 5 and 6: when the amplitude is scaled by 5, the noise diminishes by 4. One last consideration: when the lock-in low pass bandwidth gets 1000 times higher (row 2 and 6), the noise does not increase by $\sqrt{1000}$, (more or less a factor of 30), but much

Ref voltage (V)	BW (Hz)	IN range (V)	Voltage rms (nV)	$e_{n,eq}$ (nV/$\sqrt{\text{Hz}}$)	Circuit
1	1.1	2	8279	7526	1A1s, T
1	1.1	2	410	373	B, 1A2s3s, T
81 m	1.1	2	1380	1254	1A1s, T
1	1.1	81 m	319	290	B, 1A1s2s, T
5	1 k	56 m	5746	179	B, 4B1d2d, T
1	1 k	14 m	1437	45	B, 4B1d2d, T
0.1	1 k	4.7 m	812	25	B, 4B1d2d, T

Table 4.7: Output voltage noise with sinusoidal reference; the first column refers to the voltage amplitude of the signal at the DAC output; all the measurements were taken at 1 MHz.

less. Therefore, white noise is not being measured. The fifth column displays an equivalent noise spectral density, which has been evaluated by dividing the rms value by the square root of the bandwidth, as if it were white noise.

These observations suggest that phase noise is being measured. A spectral analysis of the voltage reference from the HF2LI is shown in figure 4.6a. Three different amplitudes have been analyzed: 1 V, 100 mV, and 10 mV. The typical phase noise sidebands are clearly visible; the ratio to the carrier peak is constant, for a given frequency deviation: when the amplitude scales by ten, the sideband also decreases by 20 dB, indicating that this noise is directly proportional to the signal's amplitude. The amount of phase noise affecting a sinusoidal signal is identified by the Single Sideband to Carrier Ratio (SSCR), which is the ratio of the noise power (in a bandwidth of 1 Hz), at a certain frequency deviation ω_m from the carrier ω_0, to the carrier power. It results that $SSCR(\omega_m) = S_\phi/2$, where S_ϕ is the phase noise spectral density [15]. The HF2LI user's manual indicates a −120 dBc phase noise for a 1 kHz deviation from 10 MHz (integrated over a 0.67 Hz bandwidth). Figure 4.6a is consistent with such a description, and it explains the excessive noise measured. The sidebands cannot decrease below the white noise floor, which is actually higher than 25 nV/$\sqrt{\text{Hz}}$. Figure 4.6b makes a comparison with the spectrum of a waveform generator by Agilent; the two are quite the same, so it looks useless to demand better performances to a signal generator.

The most critical aspect about phase noise is the proportionality with the voltage sinusoid amplitude. The SNR does not increase any more with the voltage, as long as the phase noise is dominant. One may ask why phase noise is concerning in a lock-in demodulation: if the two sinusoids at the multiplier's inputs share the same zero crossing fluctuations, they are always synchronous, and no phase noise should be detected. The HF2LI generates the sinusoidal reference relying on the digital samples stored in its registers, which get converted into a continuous waveform by a Direct Digital Synthesizer (DDS) along with the DAC. This analog sinusoid gets corrupted by phase noise, and, after the signal acquisition operations, it is read by the HF2LI input ADC, and finally demodulated into digital domain. The digital reference sinusoid does not experience the same corruption, so a net phase fluctuation arises.

The reference signal's noise was also studied using the lock-in itself (table

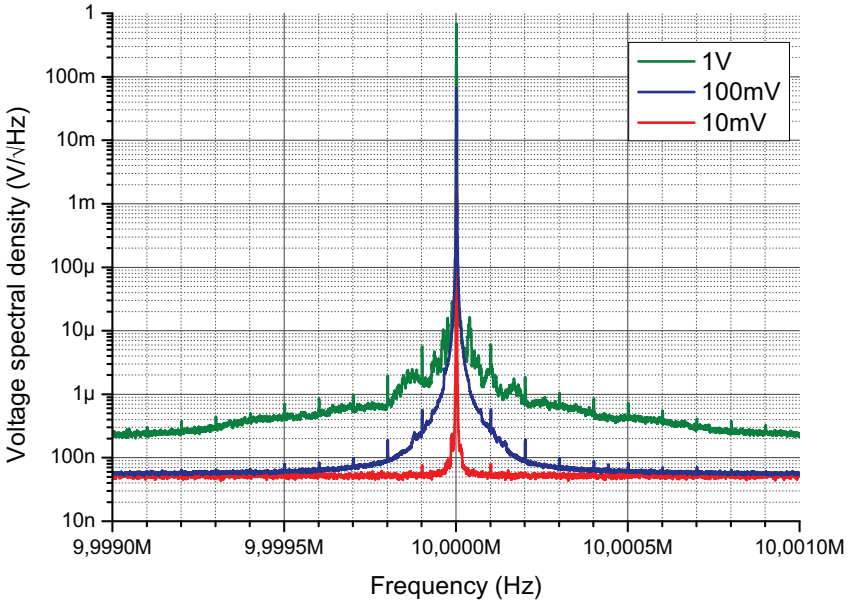

(a) *Spectrum of the voltage reference from HF2LI lock-in, for different amplitudes.*

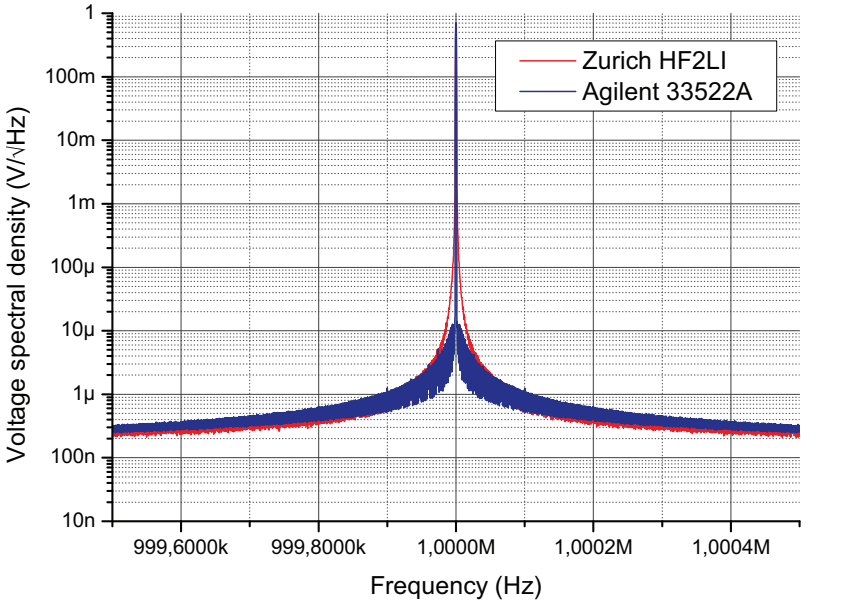

(b) *Comparison between HF2LI output and agilent 33522A waveform generator.*

Figure 4.6: Spectrum of the reference sinusoid.

Ref (V)	BW (Hz)	IN range (V)	Voltage rms (nV)	$e_{n,eq}$ (nV/$\sqrt{\text{Hz}}$)	OUT range (V)	Notes
1	1.1	2	26720	25476	1	
1	1.1	2	156	148	1	Diff
1	1.1	2	17329	16504	1	Diff, 2 gen
0.1	1.1	2	2207	2012	1	
0.1	1.1	2	81	77.1	1	Diff
0.1	1.1	0.13	1960	1867	1	
0.1	1.1	0.13	1930	1838	0.1	
10 m	1.1	0.13	219	208	0.1	
1 m	1.1	0.13	41	39	10 m	
1 m	1.1	2	240	228	10 m	
1	1.1	81 m	15126	14406	1	Diff, 2 gen
1	1.1	81 m	67.4	64.2	1	Diff
1	20	2	29365	6566	1	
1	1 k	2	33809	1069	1	
1	1.1	2	23496	22377	1	33522A
1	20	2	28254	6318	1	33522A
1	1 k	2	35512	1123	1	33522A
1	1.1	2	35811	34106	1	81150A
1	1.1	2	185	176	1	81150A, Diff

Table 4.8: HF2LI output waveform noise; all the measurements were taken at 1 MHz.

4.8), by connecting the DAC output directly to the ADC input. In a 1 Hz bandwidth, the spectral density is about 25 µV for a 1 V signal. When the amplitude is scaled by ten, also the noise scales by the same factor, coherently with figure 4.6a. To decrease the phase noise at its minimum, the amplitude was scaled to 1 mV, and the input range had to be reduced to 130 mV, otherwise the ADC input noise would have dominated (row 10 and 11); we see that the DAC white noise floor is about 40 nV/$\sqrt{\text{Hz}}$, which is also compliant with figure 4.6a.

This bottom limit is not a realistic situation, because with such a low voltage the optimum SNR would get 1000 times worse. A differential measurement is necessary to significantly reduce the reference signal's noise. The HF2LI inputs can read differential signals, so the noise rejection was tested by splitting the same output DAC to a differential input. As expected, the noise experienced a substantial reduction, even though it did not reach the noise limit of the ADC input range. A similar differential measurement was also performed: this time two different DAC outputs were sent to the same ADC differential input (row 3); a very weak attenuation was seen, perhaps indicating some correlation between the two output channels. If the noise bandwidth is increased, the rms value is not proportional to its root square, as already pointed out; it is not white noise.

The HF2LI allows to lock an external sinusoidal reference to an internal PLL, and to use it as a demodulation reference. Two external waveform generators by Agilent were tested, the 33522A and the 81150A. The external sinusoid was then sampled by the ADC, and also locked to the internal PLL, so that it would be used as a lock-in reference. Ideally, the two signals at the inputs of the multiplier

should be exactly the same, and no phase noise should be detected; actually, table 4.8 shows an unchanged situation, the external generators providing phase noise performances similar to the internal one's. After all, the ultimate phase noise source is the internal clock of the lock-in, whose jitter corrupts all the discrete-time stages; the sampled external waveform must be processed by the digital PLL, before it becomes the lock-in reference, so it might experience further clock jitter with respect to the sampled input; therefore, there is no way to cancel this phase noise with this kind of approach. The same holds if the DAC's output were reread to provide a more reliable reference.

4.3 System sensitivity

The most important result from the previous analysis is that the voltage generator noise limits the system's resolution. A differential measurement is mandatory to reach an acceptable SNR. The transimpedance output noise, with a 1 V reference, can be successfully lowered with a pair of differential sensors, provided that their matching is high; table 4.5 displays a factor of 20 noise attenuation between row 1 and 2; raising the voltage amplitude proves useless to the SNR. For a 1 kHz bandwidth, the output rms voltage noise can be 1.4 μV, which corresponds to a capacitive signal of 2.1 aF. If a margin is taken on the SNR, a 10 aF signal should be detectable with confidence.

Chapter 5

PM detection

5.1 Measurement approach

In the horizontal flow measurement, particulate matter is confined in a layer of fluid, subject to laminar flow. The motion is not perfectly horizontal, for the particle tends to drop with a sedimentation speed, which results from the balance of the all forces applied: gravity and viscous friction (the lift force can be neglected for these parameters values). In steady state condition, the sedimentation speed is equal to

$$v_z = \frac{2}{9}\frac{r^2}{\mu}(\rho_p - \rho_f)g$$

for a spherical particle, where r is the radius, μ is the fluid's viscosity, ρ_p and ρ_f are the volumic masses of the particle and of the fluid, g is the gravitational acceleration. A 10 µm plastic sphere has a 3 mm/s sedimentation speed. The horizontal speed v_x was indicatively set to 1 mm/s; therefore such a particle would immediately drop, instead of proceeding horizontally. If the diameter is halved, the sedimentation speed becomes 1/4 (still comparable to v_x), but the expected capacitive signal, less than 1 aF for a plastic sphere, decreases below the system's sensitivity. With diameters close to 1 µm the vertical speed would be sufficiently low, but the current sensitivity cannot reach such values.

The particle's speed might be increased to handle a vertical speed of 3 mm/s. The minimum length to be traveled on a single sensor is about 100 µm; if the vertical drop must be limited within 1 µm, the horizontal speed should not get below 300 mm/s. From the pulse shape section we recall that the spatial width of a pulse is of the order of 10 µm, corresponding to a 30 µs duration. Such a signal would require a 33 kHz lock-in bandwidth, a factor of 5.7^2 higher than the current value. The minimum detectable capacitance would become 12 aF, preventing even the 10 µm particle from being detected.

The sedimentation speed also depends on the fluid's density. This issue would be easily overcame by choosing a liquid medium, e.g. water. Water has a 1000 times higher volumic mass, providing a sufficient buoyancy to keep the particles on flow. Nevertheless, in-water measurements are commonly performed. We will try to measure PM in air, because it would be a much more important result.

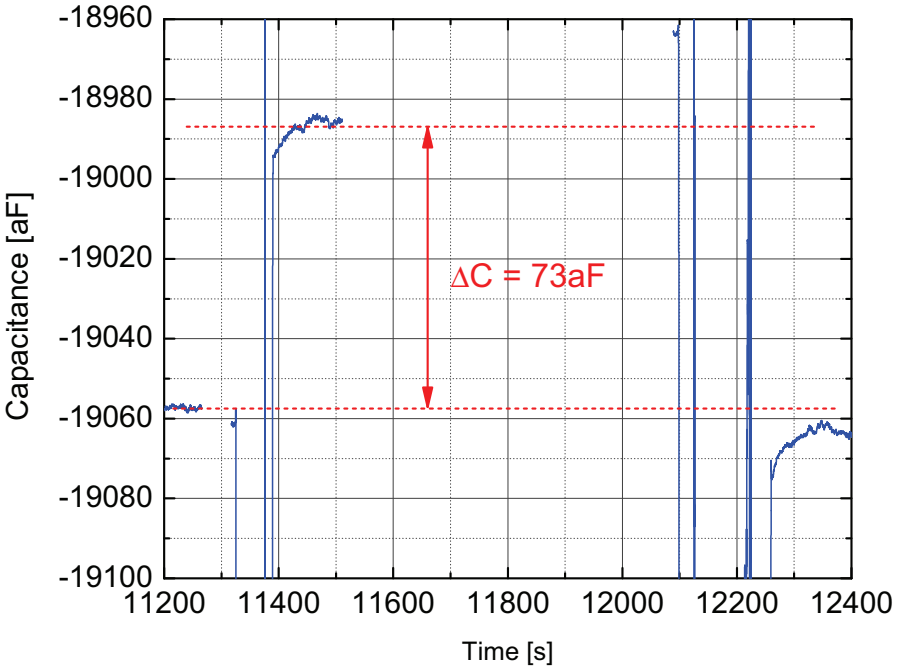

Figure 5.1: Capacitive signal due to a 20 µm plastic bead.

This compromise between measurement feasibility and resolution can be overcome by choosing a vertical fall approach: the particles would drop on the sensor, so even a steady state, narrow bandwidth measurement could be accomplished.

5.2 Static measurements

Static measurements have been carried out by positioning with accuracy single particles on a sensor; the corresponding capacitance steady state value has been compared to the initial value, thus measuring a variation. The circuit was placed on a microscope, which allowed to track the particle while it was being positioned, and to take pictures of the sensing area. Plastic beads of known diameter and permittivity (2.6) have been used; the lock-in bandwidth was set to 1.1 Hz, since steady state values had to be measured.

At first, 20 µm diameter beads were measured. The 4A4d'4d" differential pair was chosen. The conversion gain between the sensor's capacitance and the output voltage is

$$C_s = \frac{C_f}{A_0} V_{out}$$

Since the lock-in displays the output rms voltage, an additional $\sqrt{2}$ factor must be included:

$$C_s = \frac{1.4\,\text{pF}}{1\,\text{V}} \sqrt{2} V_{out,rms}$$

Of course, since the voltage transfer is a capacitive ratio, the lock-in demodulates real part of the output voltage.

Figure 5.1 shows the detected signal: three steady state intervals are visible; they are separated by high frequency signals, caused by the metal probe used to position and to remove the beads. A capacitive increase of 73 aF was measured, after two sticked beads had been placed in the middle of the 10 μm gap of sensor 4A4d', which is one of the two sensors forming the 4A4d triple. After the beads' removal, the sensor's capacitance got back to its initial value. Two pictures have been taken: after the beads' positioning (fig 5.2a), and after the removal (fig 5.2b). One bead is just in the middle of the gap, while the other is a bit outside; after the removal, they are still visible at the upper edge of the triple, far away from the gap. The signal's polarity is consistent with the arrangement: the upper electrode of the triple receives the negative voltage reference, while the lower one receives the positive. Since the initial capacitance value is negative, the lower sensor must be greater than the upper one, because the transimpedance that follows has a negative gain. The capacitive signal tends to reduce the absolute value of the overall capacitance, therefore the upper electrodes must have increased their value duo to the presence of the particles, which is just the case. To further validate this measurement, a simulation of the sensor was done, with one 20 μm plastic sphere touching the surface. The returned value is 42 aF for a single bead in the middle of the gap, in perfect agreement with the experimental result.

The second test dealt with 10 μm plastic beads (see fig. 5.4), placed on the triple 1A2d'd". This time a negative variation of 40 aF was detected. The simulation of a 10 μm bead above a 4 μm gap predicts 25 aF. At first no beads were present above the gap of the triple 1A2d (fig. 5.4a), that is the upper one; unfortunately, the manufacturing process failed to produce the electrodes with accuracy in this case, because they clearly show some unwanted ripples; this worsened the matching of the triple, resulting in a poor attenuation. Some circular dark defects in the gap area are visible, but they can be well distinguished by the spherical, transparent beads in the nearby. In the second picture (fig. 5.4b), a group of four beads appears above the upper gap, but only two seem to be in the sensitive volume, so the measured signal agrees with the simulation. In the third picture (fig. 5.4c), the group of beads has been removed; the only ones visible are not on the gap, and the measured capacitance gets back to the initial value. Again, the polarity is correct: the initial value is negative, so the upper couple, which receives the positive voltage reference, has a greater capacitance; when the beads are present, the measured value becomes more negative, therefore the upper pair's capacitance increased. The system has proven to be able to detect PM_{10}.

5.3 Dynamic measurements

An air suspension of industrial talc was created by means of an aerosol machine. This talc powder has an average 8 μm aerodynamic diameter, on a log-normal distribution, with 60% of the total being finer of 10 μm; it is composed by MgO for the 31.5 %, and by $Si0_2$ for the 62.5 %, whose permittivities are equal to 4 and 9, respectively. The particles were injected into a PDMS chamber, as depicted in figure 5.5. The inlet, decentralized from the sensors area, allowed only a

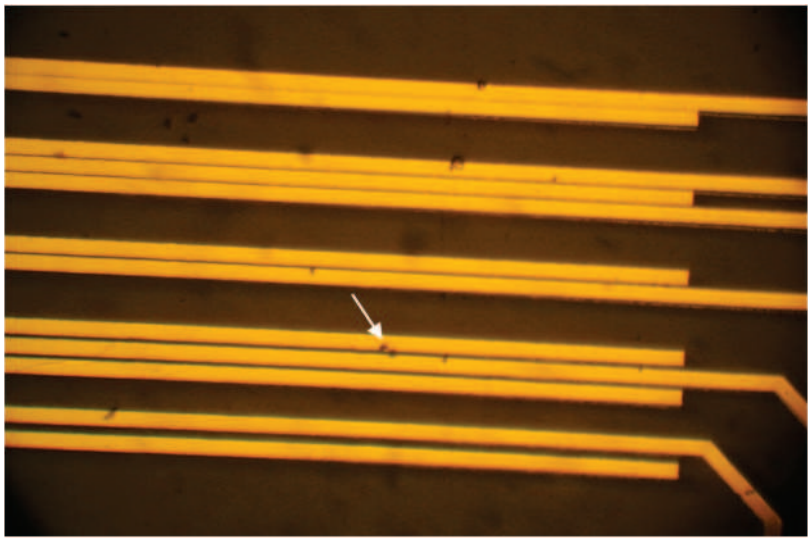

(a) *The two spheres are in the middle of the gap of sensor 4A4d'.*

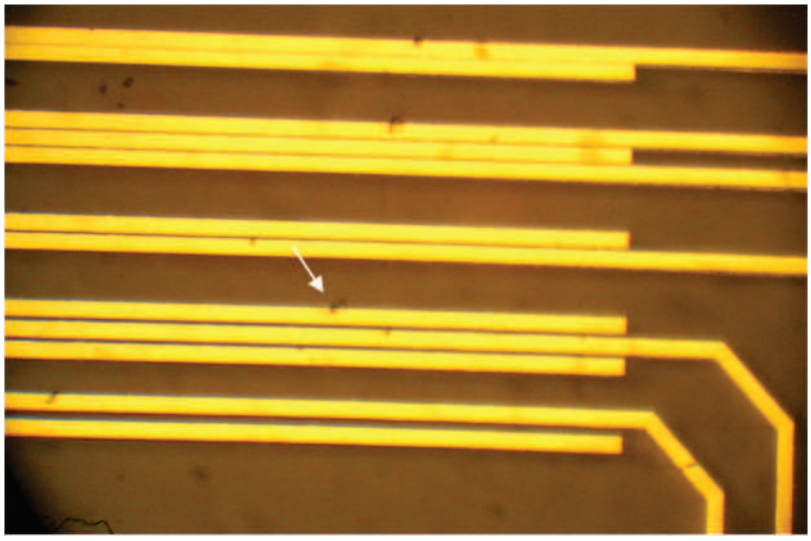

(b) *The two spheres have been removed from the gap.*

Figure 5.2: Pictures of the microscope image of sensor 4A4d'4d" during 20 µm spheres detection.

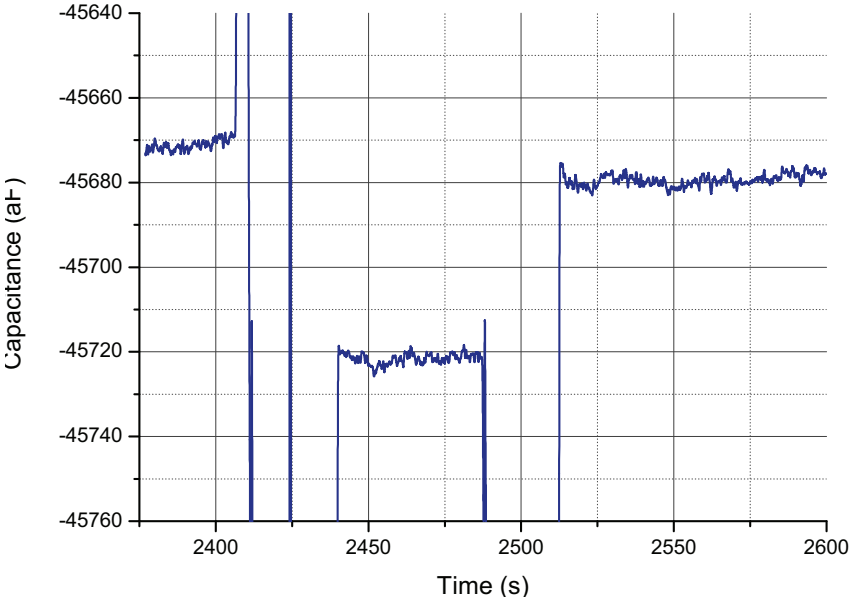

Figure 5.3: Capacitive signal due to a 10 µm plastic bead.

thin, mono-particle layer of talc to reach the active electrode pair, with a certain concentration. The particles deposition was sensed in real time, so a minimum 100 Hz lock-in bandwidth was chosen.

The differential pair 2B-2s3s was used at first. The measurement results are listed in table 5.1; the net capacitive signal is the difference between the sensors initial capacitance (for the differential pair 2B-2s3s it equals 14 fF, while for a single sensor it could be 500 fF), and the steady state value after the aerosol machine was turned off, when all the talc particles settled on the surface. Figure 5.6a shows the first measurement: a positive net signal of 100 aF was detected. The transient is characterized by a certain granularity: a series of smaller capacitive steps, either positive or negative, suggest that the talc particles drop quite randomly on both the electrodes; some major steps can be identified, cor-

Attempt	Net signal (aF)	Sensor	BW (Hz)	Gap (µm)
1	100	2D-2s3s	100	4
2	-15	2D-2s3s	100	4
4	15	2D-2s3s	100	4
9	-80(x2)	2D-2s3s	1 k	4
11	-10	2D-2s3s	1 k	4
12	-100	2D-1s	1 k	4
18	-170	2D-3d	100	6

Table 5.1: Series of dynamic measurements; the capacitive signal is in good agreement with the microscope photographs.

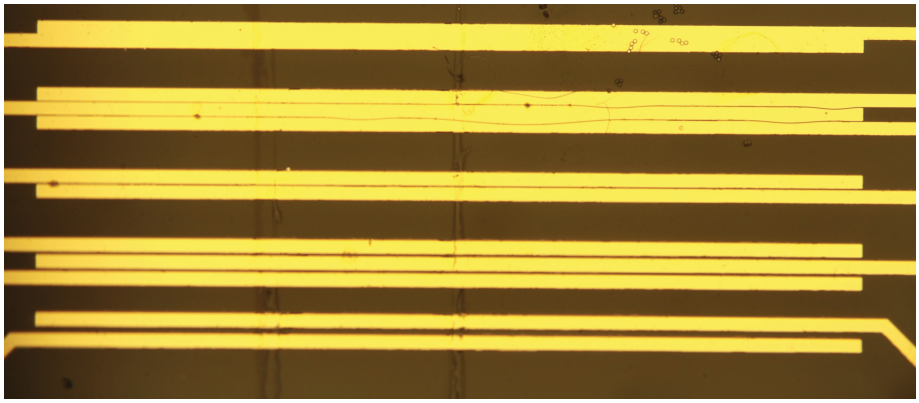

(a) *No beads on electrodes 1A2d.*

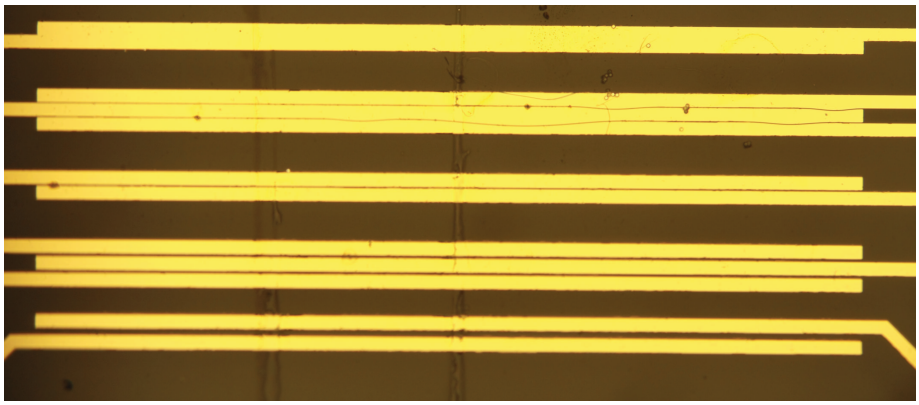

(b) *Four beads in the gap area of electrodes 1A2d'.*

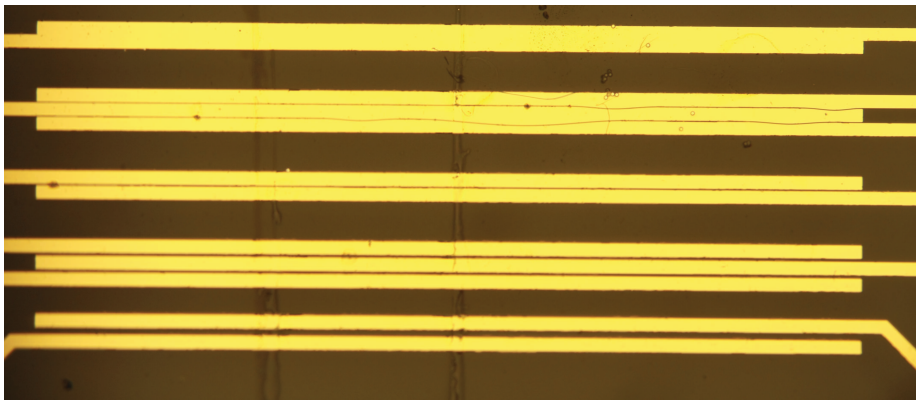

(c) *The group of beads has been removed.*

Figure 5.4: Microscope pictures of the bipolar signal.

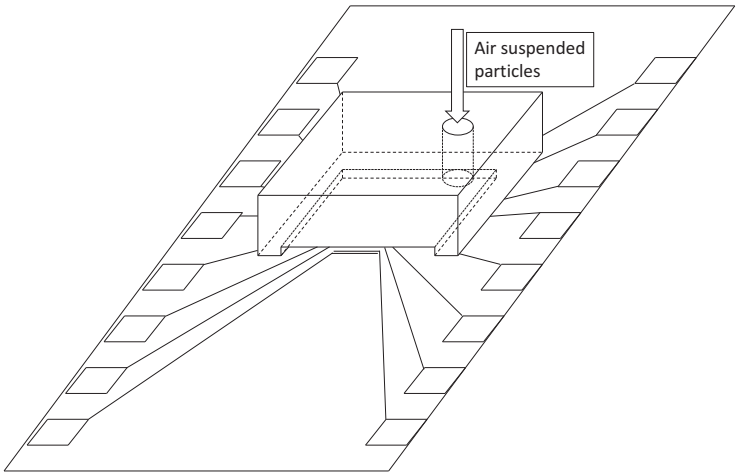

Figure 5.5: Microfluidic chamber for air suspended particles measurement.

responding to bigger particles; during the transient, even 10 aF steps are visible.

The second measurement shows a net 15 aF step, followed by a non-monotone transient, probably due to the tail of particles which are slower to settle. Measure 4 can be also quantified in a net 15 aF step, but positive. The transient shows two (or three) successive signals, the former rising by 25 aF, the latter decreasing by 10 aF.

Perhaps the most interesting measurement is number 9. Two, well separated, −80 aF steps can be distinguished; figure 5.7c is a photograph of the electrodes. Two greater grains are visible on the right side of electrode 3s, likely the cause of these two steps. Other smaller particles were spread uniformly, and the concentration was low enough to distinguish all of them. Figure 5.7b highlights an inner step of −20 aF, right after the first major step.

Measurement number 11 is quite interesting: although the net signal remains within 10 aF, the transient displays a series of multiple bipolar signals, which also include some 40 aF steps.

The last two measurements were performed with a single electrode, therefore without input noise reduction. The initial capacitance is now of the order of hundreds of fF, and signals of hundreds of aF were measured.

The minimum detected signal was 10 aF, lower than the signal produced by a single 10 µm bead during the static measurements; the dielectric constant of talc powder is also higher than polystyrene's, so we may conclude that particles with diameter lower than 10 µm were detected.

5.4 Conclusions

The design of this particulate matter detector ended successfully. Two remarkable accomplishments can be highlighted: it has been proven that particulate

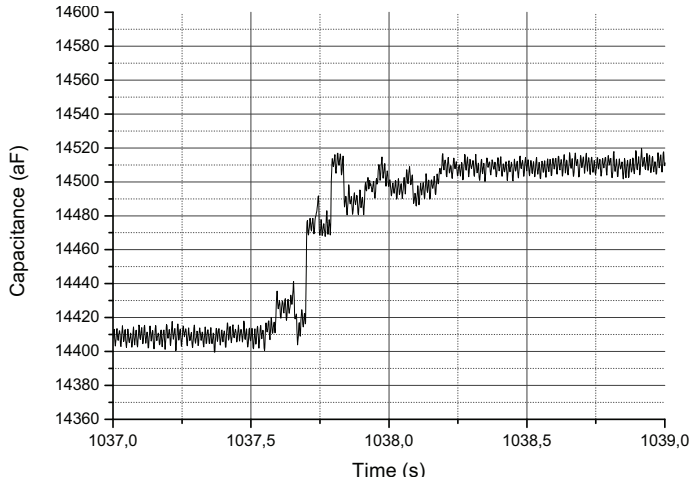

(a) *Measure 1.*

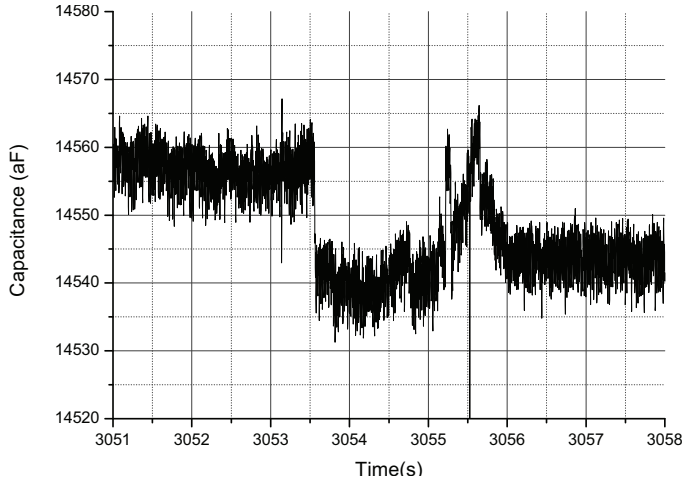

(b) *Measure 2.*

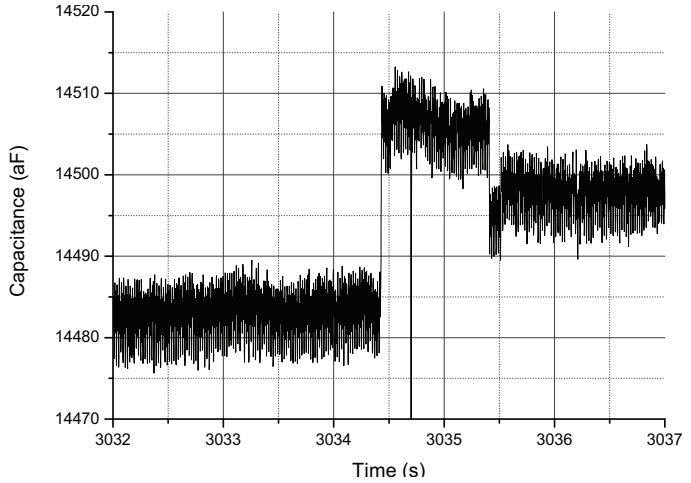

(c) *Measure 4.*

Figure 5.6: Sensor capacitance after lock-in demodulation.

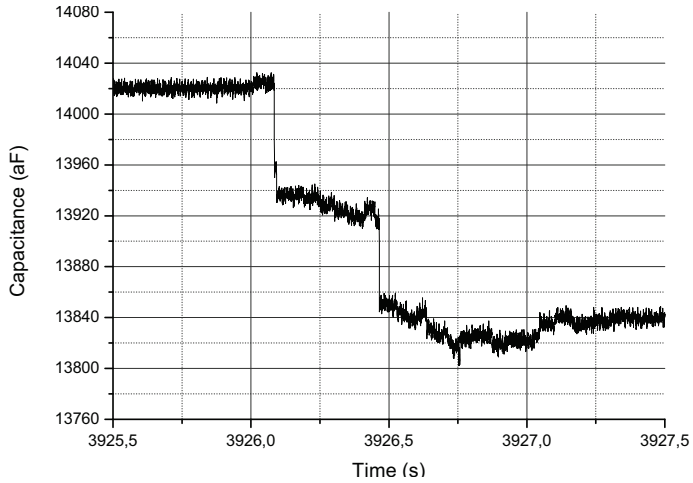

(a) *Measure 9.*

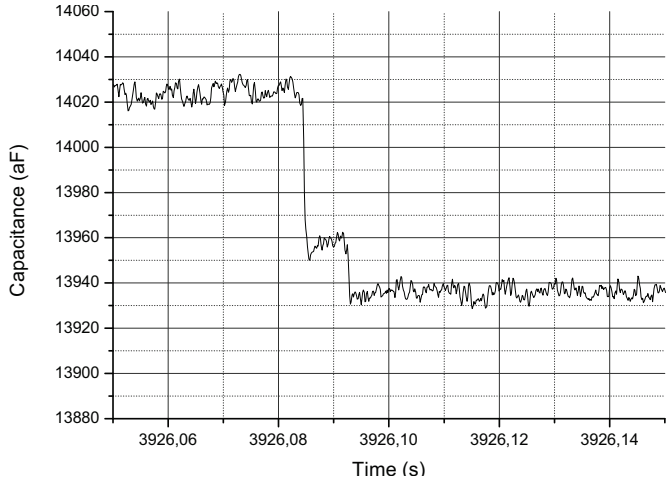

(b) *Measure 9 (detail).*

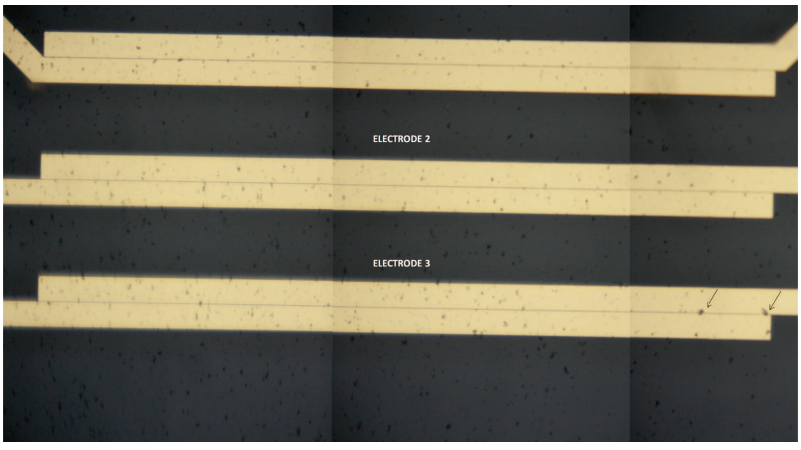

(c) *Measure 9 (electrodes).*

Figure 5.7: Sensor capacitance after lock-in demodulation.

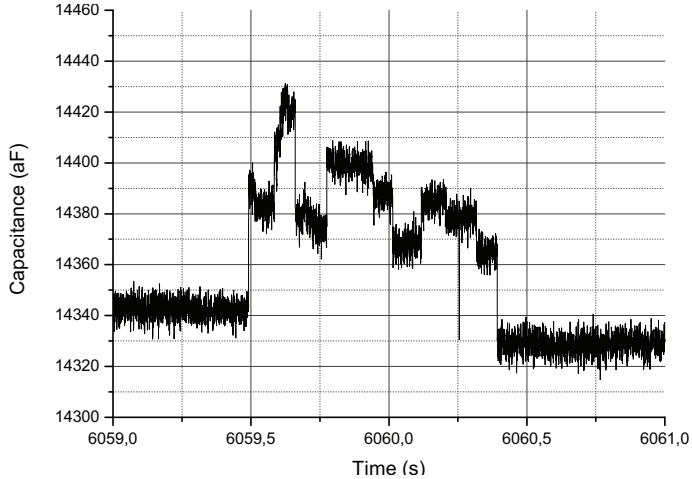

(a) *Measure 11.*

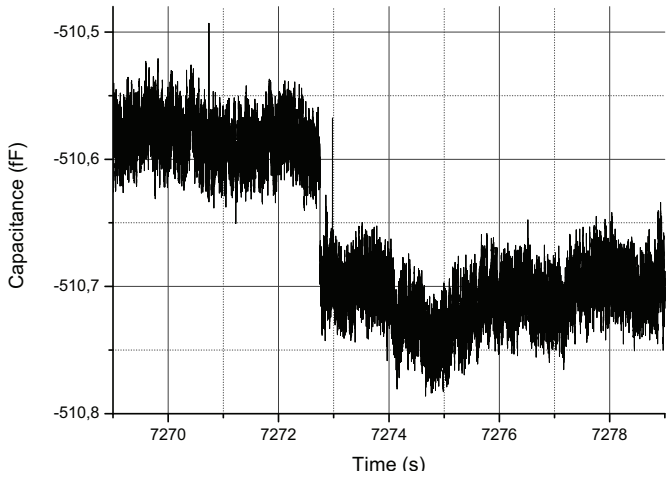

(b) *Measure 12.*

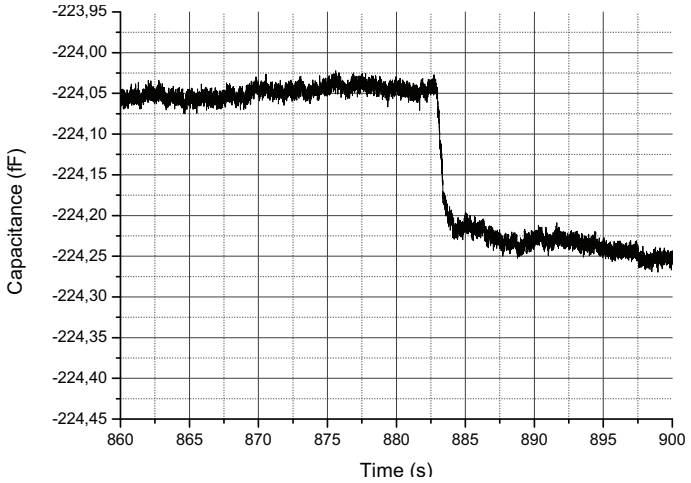

(c) *Measure 18.*

Figure 5.8: Sensor capacitance after lock-in demodulation.

matter can be detected by capacitive impedance measurements, the system being able to reveal single particles of the PM_{10} fraction, at least; it has been proven that this kind of measurement can be done directly in the air.

The initial goal to build a compact module able to perform the whole measurement has not been fully achieved. There are some major issues that make the single particle counting, with diameter sorting, a difficult task. The horizontal flow approach turned out to be impracticable, due to the sedimentation speed. Only the smaller particles can float adequately, but the current sensitivity cannot sense them. A vertical fall approach was chosen, but the $PM_{2.5}$ is still beyond the system's capability.

The total sensor capacitance was ignored during the design process, but it eventually emerged as the cause of the input noise transfer, which was the main contribution in the SNR, because of the phase noise accompanying the voltage reference. After all, there are five or six orders of magnitude between the capacitive signal and the total sensor's capacitance: the voltage reference has to guarantee a 100 to 120 dB dynamic, which is a quite extreme requirement. It would have been much simpler to limit the sensor's capacitance in the layout process: thinner and shorter electrodes, stray insensitive traces geometry, and differential pairs only.

The horizontal flow approach allows to count single particles without losing anyone (within the sensitivity limit), because PM has to cross the sensor. Conversely, in the proposed vertical flow approach, the particles are required to fall exactly in correspondence of the gap: a consistent fraction gets lost. Of course, the geometry can be optimized to reduce the inefficient area, by adopting interdigitated configurations that cover the whole sensor surface. Or, instead of capacitive electrodes, a CCD matrix could be an alternative sensor: the PM would cover a certain number of pixels, also giving direct information on the diameter, and no particle would be lost. Anyhow, the particles dropped on the sensor must be removed in some way, otherwise the surface would saturate. A possible solution could be the ultrasonic removal.

An integrated sensor along with the acquisition and demodulation stages will be the next step, thanks to the MEMS technology. The sensor may be added above the electronics area, or aside. The integrated manufacturing process provides a higher lithographic resolution, at least 1 μm; electrodes separated by a narrower gap could be fabricated, resulting in a higher transduction gain. A huge advantage would result by the extreme reduction of parasitic capacitances, allowing to reach the 10 zF sensitivity: the $PM_{2.5}$ and the sub-micron detection would be the next challenges.

An example of successful air microfluidic particulate sorting is described by Papotny *et al.* [14]. Once the particles have been divided by size, an array of custom, parallel-plate sensors would sense them, as was done by Kawaguchi *et al.* for 300 nm pollen measurement [17]. Anyway, because of the fluidodynamic issues of the horizontal flow, an interdigitated electrodes array for vertical fall will be realized, as a first attempt for a fully integrated system.

Acknowledgements

I would like to acknowledge my family: my parents Biagio and Ida, and my brother Federico. They've allowed me to live this very important formative experience with the maximum tranquility and freedom, providing the necessary financial support, and always being close to me; this accomplishment would have never been achieved without them; my girlfriend Yelena: besides being extremely encouraging, since I met her, I have changed my point of view on many things, which also include university, and she is a fundamental part of my life and of my choices; Prof. Marco Sampietro, who gave me the opportunity to work on a novel and interesting project, always trusting his students, and making the right decision whenever necessary; Ing. Marco Carminati, who supervised me through the whole work, establishing a friendly cooperation; Prof. Giorgio Ferrari, who took part to the project, always sharing a part of his time with whoever needed an advice, having everything clear in his mind; Ing. Elena Bianchi, Ing. Francesca Nason, Prof. Luca Cortelezzi (from McGill University), Prof. Gabriele Dubini: they designed a reliable micro-fluidodynamic system, which proved to be very critical; my friends Ema, Caste and Scotti, for the experiances I have shared and the time I have spent with them, and for that will be spent; my university mates Ose, Fabio, Paolo, Tiziano, Luca, Pietro, whom I shared this path with, the laboratory mates Giacomo, Ibrahim, Davide, Andrea G. and Andrea R., Giovanni, the researchers Ing. Maddalena Binda and Prof. Dario Natali: I wish the best to all of them.

Bibliography

[1] Zereini F., Wiseman C. L. S., *Airborne Particulate Matter: Sources, Composition and Concentrations*, Springer (2010).

[2] Marcazzan G. M., Vaccaro S., Valli G., Vecchi R., *Characterization of PM10 and PM2.5 particulate matter in the ambient air of Milan (Italy)*, Atmospheric Environment 35 (2001) 4639–4650.

[3] *Basic Guide to Particle Counters and Particle Counting*, Particle Measuring Systems, Inc. (2011).

[4] Baron P. A., Kulkarni P., Willeke K., *Aerosol Measurement: Principles, Techniques, and Applications*, Wiley (2011).

[5] Ashok A., Barrett S. R. H., Caiazzo F., Waitz I. A., Yim S. H. L. , *Air pollution and early deaths in the United States. Part I: Quantifying the impact of major sectors in 2005*, Atmospheric Environment 79 (2013) 198e208.

[6] Carminati M., Sampietro M., Carminati G., *Analysis of Instrumentation Performance for Distributed Real-Time Air Quality Monitoring*

[7] Vecchi R., *Il particolato atmosferico: la composizione elementare*

[8] Carminati M., *Instrumentation for electrical detection in biology and nanoelectrochemistry*, Doctoral Dissertation (2009).

[9] Meade M., *Lock-in amplifiers: principles and applications*, IEE electrical measurement series, P. Peregrinus on behalf of the Institution of Electrical Engineers (1983).

[10] Alagna D., *Sistema di Generazione ed Acquisizione con Elaborazione Real-Time su FPGA per Misure Elettrochimiche*, MSc Dissertation (2011).

[11] Carminati M., Ferrari G., Sampietro M., *Attofarad resolution potentiostat for electrochemical measurements on nanoscale biomolecular interfacial systems*, Rev. Sci. Instrum. 80, 124701 (2009).

[12] Rottigni A., *Electronical instrumentation for impedance measurement on biosamples*, Doctoral Dissertation (2012).

[13] Chen J. Z., Darhuber A. A., Troian S. M., Wagnera S., *Capacitive sensing of droplets for microfluidic devices based on thermocapillary actuation*, Lab Chip 4 (2004) 473-480.

[14] Paprotny I., Doeringa F., Solomonc P. A., Whitea R. M., Gundelb L. A., *Microfabricated air-microfluidic sensor for personal monitoring of airborne particulate matter: Design, fabrication, and experimental results*, Sens. Actuators A: Phys. (2013), http://dx.doi.org/10.1016/j.sna.2012.12.026

[15] Lacaita A. L., Levantino S., Samori C., *Integrated Frequency Synthesizers for Wireless Systems*, Cambridge (2007).

[16] Bolzern P., Scattolini R., Schiavoni N., *Fondamenti di controlli automatici*, McGraw-Hill (2008).

[17] Kawaguchi C., Noda T., Tsutsui M., Taniguchi M., Kawano S., Kawaii T., *Electrical detection of single pollen allergen particles using electrode-embedded microchannels*, J. Phys.: Condens. Matter 24 (2012).

[18] Bernardoni V., Vecchi R., Valli G., Piazzalunga A., Fermo P., *PM10 source apportionment in Milan (Italy) using time-resolved data*, Science of the Total Environment 409 (2011) 4788–4795.